

X-RAY EMISSION FROM ACTIVE GALACTIC NUCLEI WITH INTERMEDIATE MASS BLACK HOLES

G. C. DEWANGAN¹, S. MATHUR², R. E. GRIFFITHS¹, & A. R. RAO³

Draft version

ABSTRACT

We present a systematic X-ray study of eight active galactic nuclei (AGNs) with intermediate mass black holes ($M_{BH} \sim 8 - 95 \times 10^4 M_{\odot}$) based on 12 *XMM-Newton* observations. The sample includes the two prototype AGNs in this class – NGC 4395 and POX 52 and six other AGNs discovered with the Sloan Digitized Sky Survey. These AGNs show some of the strongest X-ray variability with the normalized excess variances being the largest and the power density break time scales being the shortest observed among radio-quiet AGNs. The excess variance – luminosity correlation appears to depend on both the BH mass and the Eddington luminosity ratio. The break time scale – black hole mass relations for AGN with IMBHs are consistent with that observed for massive AGNs. We find that the FWHM of the H β /H α line is uncorrelated with the BH mass, but shows strong anticorrelation with the Eddington luminosity ratio. Four AGNs show clear evidence for soft X-ray excess emission ($kT_{in} \sim 150 - 200$ eV). X-ray spectra of three other AGNs are consistent with the presence of the soft excess emission. NGC 4395 with lowest L/L_{Edd} lacks the soft excess emission. Evidently small black mass is not the primary driver of strong soft X-ray excess emission from AGNs. The X-ray spectral properties and optical-to-X-ray spectral energy distributions of these AGNs are similar to those of Seyfert 1 galaxies. The observed X-ray/UV properties of AGNs with IMBHs are consistent with these AGNs being low mass extension of more massive AGNs; those with high Eddington luminosity ratio looking more like narrow-line Seyfert 1s while those with low L/L_{Edd} looking more like broad-line Seyfert 1s.

Subject headings: accretion, accretion disks — galaxies: active – galaxies: Seyfert — X-rays: galaxies

1. INTRODUCTION

The existence of astrophysical black holes in two mass ranges, stellar mass black holes with $\sim 10M_{\odot}$ in X-ray binaries and supermassive black holes (SMBHs) with masses in the range of $\sim 10^6 - 10^9M_{\odot}$ at the centers of active galaxies, is well supported by observations. Intermediate mass black holes (IMBHs), bridging the gap between the stellar mass and supermassive black holes, remain relatively unexplored. There was no observational evidence for such black holes for many years. Recent optical and X-ray observations have revived the possibility of existence of IMBHs. There are indirect evidence for IMBHs with masses of $\sim 10^4 - 10^6M_{\odot}$ at the center of some galaxies based on radiative signatures or dynamical measurements (Filippenko & Ho 2003; Barth et al. 2004; Greene & Ho 2004, 2007a). The AGNs with IMBHs form an important class for a number of reasons. First, the growth of SMBHs in Seyfert galaxies and quasars is still not understood. The nature of seed black hole (BH) is the major challenge to any cosmological BH growth model. Observations of IMBHs at the dynamical centers of nearby galaxies would provide significant constraints on the nature of seed black holes for cosmological growth models. The $M_{BH} - \sigma_*$ relation strongly suggests co-evolution of galaxies and BHs, but it is not known if this relation is established early in the evolution process. If

this relation is established late in the galaxy evolution, as suggested by Di Matteo et al. (2003), then we should see deviations in the $M_{BH} - \sigma_*$ relation in a population of IMBHs that is not yet fully grown. In this growing phase, the accretion process and the disk-corona geometry around the central IMBH could be markedly different than that around SMBHs in luminous AGNs. Therefore, it is crucial to study accretion onto the least massive central BHs in galaxies. AGNs with IMBHs also provide the missing link between the stellar mass and SMBHs and enable us to test if the accretion physics is the same at all scales. They will also help to understand the accretion physics as it would be easier to isolate certain characteristics arising solely from an extreme physical parameter, in this case, low mass BH. AGNs with IMBHs may reveal new accretion phenomena depending on the mode of accretion at low BH masses. It is also possible that they pass through an active phase of accretion and contribute to the observed background radiation at some level, particularly to the X-ray background. The mergers of intermediate mass black holes with masses 10^5M_{\odot} are expected to provide strong signals of gravitational waves for the *Laser Interferometric Space Antenna* (e.g., Hughes 2002).

The two prototypes examples of IMBH AGNs are the late-type spiral galaxy NGC 4395 (Filippenko & Ho 2003) and the dwarf elliptical galaxy POX 52 (Barth et al. 2004). Greene & Ho (2004) discovered 19 such AGNs using the Sloan Digital Sky Survey (SDSS). They have increased their sample by an order of magnitude to 174 using the fourth data release of the SDSS (Greene & Ho 2007a). NGC 4395 has the emission properties of a type 1 AGN, with broad optical and UV emission

¹Department of Physics, Carnegie Mellon University, 5000 Forbes Avenue, Pittsburgh, PA 15213 USA; email: gulabd@cmu.edu, griffith@astro.phys.cmu.edu ²Astronomy Department, The Ohio State University, 140 West 18th Avenue, Columbus, OH 43210, USA ³Department of Astronomy and Astrophysics, Tata Institute of Fundamental Research, Mumbai 400005, India

lines and a point-like hard X-ray source. Its X-ray emission is extremely rapidly variable (see e.g., Vaughan et al. 2005). Filippenko & Ho (2003) argued that the true mass of the black hole is likely to be $\sim 10^4 - 10^5 M_\odot$, while reverberation mapping of NGC 4395 has provided a BH mass of $(3.6 \pm 1.1) \times 10^5 M_\odot$ (Peterson et al. 2005). Another recently discovered AGN with an IMBH is POX 52, a dwarf elliptical galaxy at $z = 0.021$. It was discovered in an objective-prism search for emission line objects by Kunth et al. (1981) who also noted its star-like appearance in the Palomar Sky Survey images. Follow-up imaging and spectroscopic observations by Kunth et al. (1987) revealed a dwarf galaxy with an AGN spectrum. The object was classified as a Seyfert 2 galaxy by Kunth et al. (1981) based on the flux-ratios of narrow emission lines although a weak broad component of the $H\beta$ line was seen with a full width at half maximum, FWHM $\sim 840 \text{ km s}^{-1}$. The galaxy is indeed quite small with a diameter $\sim 6.4 \text{ kpc}$ and its absolute magnitude is only $M_V = -16.9$. The luminosity of the nucleus is comparable to that of a mild Seyfert 2 nucleus but the ratio of nuclear to host-galaxy luminosity is 1.1, a typical value for quasars (Kunth et al. 1987). Barth et al. (2004) obtained a high quality optical spectra of POX 52 at the Keck that revealed an emission line spectrum very similar to that of the dwarf Seyfert 1 galaxy NGC 4395, with broad components to the permitted lines and reclassified POX 52 as a Seyfert 1 galaxy. This galaxy has a central velocity dispersion of 36 km s^{-1} , which yields a mass of $1.4 \times 10^5 M_\odot$, again consistent with that derived from the $H\beta$ line width (Barth et al. 2004).

AGNs with IMBHs are rare compared to luminous AGNs. One explanation is that they are short-lived. Presumably, all AGNs grow fast in their early phase until their BH mass increases to $10^6 M_\odot$. During this fast-growth phase, the accretion rate may be close to Eddington or super-Eddington. The relative accretion rates of ~ 1 for the SDSS AGNs with IMBH, derived by Greene & Ho (2004) from the optical data, favors the above scenario. However, all AGNs with IMBH are not accreting at high rates e.g., NGC 4395 is underluminous for its BH mass with $L/L_{Edd} \sim 1.2 \times 10^{-3}$ (Peterson et al. 2005) or at most 0.2 (Vaughan et al. 2005). In fact, very little is known about the accretion process onto IMBHs in AGNs. The only AGN that has been well studied in X-rays is NGC 4395. Iwasawa et al. (2000) presented the ASCA spectrum that showed a power-law continuum of photon index $\Gamma = 1.7 \pm 0.3$ with a Fe K line marginally detected at $\sim 6.4 \text{ keV}$. The soft-X-ray emission below 3 keV is strongly attenuated by absorption. The X-ray spectrum in this absorption band showed a dramatic change in response to the variation in continuum luminosity. Iwasawa et al. (2000) concluded that the nuclear source of NGC 4395 is consistent with a scaled-down version of higher-luminosity Seyfert nuclei. Vaughan et al. (2005) have studied the exceptional X-ray variability of NGC 4395. The variations observed are among the most violent seen in an AGN to date, with the fractional rms amplitude exceeding 100% in the softest band.

Greene & Ho (2007b) have performed snapshot (5 ks exposure) *Chandra* ACIS X-ray observations of IMBH AGNs discovered with SDSS. They detected 8 of the 10 AGNs with IMBH with a significance $\geq 3\sigma$. They

measured the 0.5 – 2 keV photon indices in the range of 1 – 2.7, consistent with that for luminous AGNs, implying that the BH mass is not the fundamental driver for the soft X-ray spectral shape. However, this result is not robust as some of the measurements are based on hardness ratios. Moreover, with 5 ks *Chandra* exposures, it was not possible to make detailed spectral and temporal analysis of any of the AGNs.

In this paper, we present X-ray temporal and spectral study of a sample of 8 AGNs with IMBHs. These AGNs with $M_{BH} < 10^6 M_\odot$ were selected based on the availability of *XMM-Newton* data. In Table 1, we list these AGNs along with their general properties. The least massive AGN in our sample has only $M_{BH} \sim 83000 M_\odot$. The accretion rates of these AGNs, estimated from optical observations, has a large range ($L_{bol}/L_{Edd} \sim 10^{-3} - 3$), suggesting a large diversity in the X-ray properties of these AGNs. We also present optical/UV emission observed with *XMM-Newton* optical monitor (OM). We describe *XMM-Newton* observations and data reduction in Section 2. In Section 3, we present temporal analysis of the EPIC-pn data, followed by spectral analysis in Section 4. We present the analysis of OM data and derive optical-to-X-ray spectral indices (α_{ox}) in Section 5. We discuss the results in Section 6, followed by a summary of our study in Section 7.

We assume the following cosmological parameters to calculate distances; $H_0 = 71 \text{ km s}^{-1} \text{ Mpc}^{-1}$, $\Omega_m = 0.27$, and $\Omega_\Lambda = 0.73$. In the following, we abbreviate the names of the AGNs with IMBHs discovered with the SDSS e.g., we mention SDSS J082912.67+500652.3 as J0829+5006.

2. OBSERVATION & DATA REDUCTION

All the eight AGNs with IMBHs presented here were observed with *XMM-Newton* between 2002 May and 2006 April. The European Photon Imaging Cameras (EPIC) pn (Strüder et al. 2001) and MOS (MOS1 and MOS2; Turner et al. 2001) were operated in the imaging mode during all the observations. Table 2 lists the details of the X-ray observations. NGC 4395, J0829+5006 and J1357+6525 were observed multiple times. The observation data files were processed to produce calibrated event lists using the Science Analysis System (SAS v7.0.0). Examination of the background rate above 10 keV showed that the first observation of NGC 4395 on 2002 June and the first, second and fourth observations of J0829+5006 were completely swamped out by the flaring particle background and therefore these observations were discarded from further study. The rest of observations were either clean or partly affected by the particle background and the intervals of high particle background were discarded from spectral analysis. We extracted the source spectra using the good EPIC-pn events in circular regions of radii in the 25 – 40'' centered at the source position. We used event with pattern 0 – 4 (single and double pixel events) for all observations except for the long observation of NGC 4395. We used only the single pixel events for the long $\sim 100 \text{ ks}$ observation of NGC 4395. The background spectra were similarly extracted from nearby circular regions free of sources. Spectral response files were generated using the SAS tasks ‘rmfgen’ and ‘arfgen’. In Table 1, we have listed the ‘cleaned’ exposure obtained from the EPIC-pn spectra. For temporal

TABLE 1
GENERAL PROPERTIES OF AGN WITH INTERMEDIATE MASS BLACK HOLES OBSERVED WITH *XMM-Newton*

Object	Position		Redshift (<i>z</i>)	Galactic N_H (10^{20} cm $^{-2}$)	FWHM(km s $^{-1}$) ($H\alpha$ or $H\beta$)	$M_{BH}(M_\odot)$	$\frac{L_{bol}}{L_{Edd}}$	Reference
	α (J2000.0)	δ (J2000.0)						
NGC 4395	12 25 48.93	+33 32 47.8	0.001	1.85	1500	3.6×10^5	1.2×10^{-3}	(1)
POX 52	12 02 56.90	-20 56 03.0	0.021	3.85	760	1.6×10^5	0.5 – 1	(2)
SDSS J010712.03+140844.9	01 07 12.03	+14 08 44.9	0.0768	3.44	830	7.2×10^5	1.24	(3)
SDSS J024912.86-081525.6	02 49 12.86	-08 15 25.6	0.0295	3.67	732	8.3×10^4	0.71	(3)
SDSS J082912.67+500652.3	08 29 12.67	+50 06 52.3	0.0434	4.08	870	5.2×10^5	0.95	(3)
SDSS J114008.71+030711.4	11 40 08.71	+03 07 11.4	0.0811	1.91	591	5.9×10^5	2.98	(3)
SDSS J135724.52+652505.8	13 57 24.52	+65 25 05.8	0.106	1.36	872	9.5×10^5	1.21	(3)
SDSS J143450.62+033842.5	14 34 50.71	+03 38 40.4	0.0284	2.43	1089	2.0×10^5	0.33	(3)

References: (1) Peterson et al. (2005), (2) Barth et al. (2004) (3) Greene & Ho (2004).

TABLE 2
LOG OF *XMM-Newton* OBSERVATIONS

Object	ObsID	Start date	pn rate (counts s $^{-1}$)	pn exposure (ks)
NGC 4395	0112522001(1)	2002-06-12		
	0112521901(2)	2002-05-31	0.56 ± 0.007	12.5
	0142830101(3)	2003-11-30	1.13 ± 0.004	93.0
	0112522701(4)	2003-01-03	1.14 ± 0.014	5.9
POX 52	0302420101(1)	2005-07-08	0.05 ± 0.001	81.1
	J0107+1408	0305920101(1)	0.27 ± 0.003	24.9
J0249-0815	0303550101(1)	2006-02-16	0.23 ± 0.008	4.0
	J0829+5006	0303550301(1)	2006-03-27	
0303550801(2)		2006-03-28		
0303550901(3)		2006-04-26	0.95 ± 0.02	2.3
0303551001(4)		2006-04-26		
J1140+0307	0305920201(1)	2005-12-03	0.66 ± 0.004	35.1
	J1357+6525	0305920301(1)	2005-04-04	0.45 ± 0.005
0305920501(2)		2005-05-16	0.55 ± 0.01	1.9
0305920601(3)		2005-06-23	0.42 ± 0.006	12.0
J1434+0338	0305920401(1)	2005-08-18	0.10 ± 0.002	22.0

analysis we considered the full lengths of the observations after correcting for the varying background rate. The source and background lightcurves were extracted using EPIC-pn events with pattern 0 – 12 and similar extraction regions described above. The source lightcurves were corrected for background contributions and telemetry dropouts.

The optical/UV monitor, co-aligned with the X-ray telescopes, was operated in the imaging mode utilizing one or more optical/UV filters, thus providing simultaneous optical/UV/X-ray coverage. The OM data were processed with the SAS task ‘omichain’.

3. TEMPORAL ANALYSIS

The background-corrected EPIC-pn lightcurves of the eight AGNs are shown in Figure 1 with 300 s bins. There are two lightcurves for each of NGC 4395 and J1357+6525 extracted from different observations. All AGNs exhibit strong and rapid X-ray variability. Individual AGNs show different amplitudes of variability. The most remarkable variability is seen in the lightcurve of NGC 4395. X-ray emission from Pox 52 is also highly variable. The 0.2 – 10 keV band light curve shows a trough-to-peak variations by a factor of ~ 10 . There are several rapid variability events e.g., roughly one event in every 10000 s, throughout the observations. The count rate is found to increase by a factor $\gtrsim 2$ in ~ 2500 s in these events. The most dramatic event is seen near the start of the observation. The count rate increased by a factor of ~ 2 and decreased immediately by a factor ~ 3 in an interval of about ~ 5400 s. To quantify the variability properties of indi-

vidual AGNs, we have measured the intrinsic source variability expressed in terms of the excess variance ($\sigma_{X,S}^2$) i.e., the variance after subtracting the contribution expected from measurement errors, the normalized excess variance ($\sigma_{N,X,S}^2 = \sigma_{X,S}^2/\bar{x}^2$ with \bar{x} is the mean count rate) and the fractional root mean square (rms) variability amplitude ($F_{var} = \sqrt{\sigma_{N,X,S}^2}$) (see Vaughan et al. 2003 and references therein). These quantities are listed in Table 3 for each lightcurve. NGC 4395 in the third observation and POX 52 show the largest fractional variability amplitudes of $65.6 \pm 4.0\%$ and $73.6 \pm 9.3\%$, respectively. The fractional variability amplitude of NGC 4395 calculate here is similar within errors to that calculated by Vaughan et al. (2005) who have performed a detailed analysis of temporal characteristics of NGC 4395 using the third *XMM-Newton* observation. Vaughan et al. (2005) also measured the the soft (0.2 – 0.7) band F_{var} to be in excess of unity, making NGC 4395 the most variable AGN. In the case of POX 52, some contribution to the large F_{var} may arise from incorrect background correction as the long observation was partly affected with flaring background (see below).

One of the objectives of this paper is to compare the variability characteristics of AGNs with IMBHs with that of NLS1s and broad-line Seyfert 1 galaxies (BLS1s). Leighly (1999a) presented a comprehensive X-ray variability of a sample of NLS1s based on *ASCA* observations. Nandra et al. (1997) presented a systematic time series analysis of Seyfert 1 galaxies consisting mostly of BLS1s using *ASCA* data. It is preferable to use results based on *XMM-Newton* observations. However,

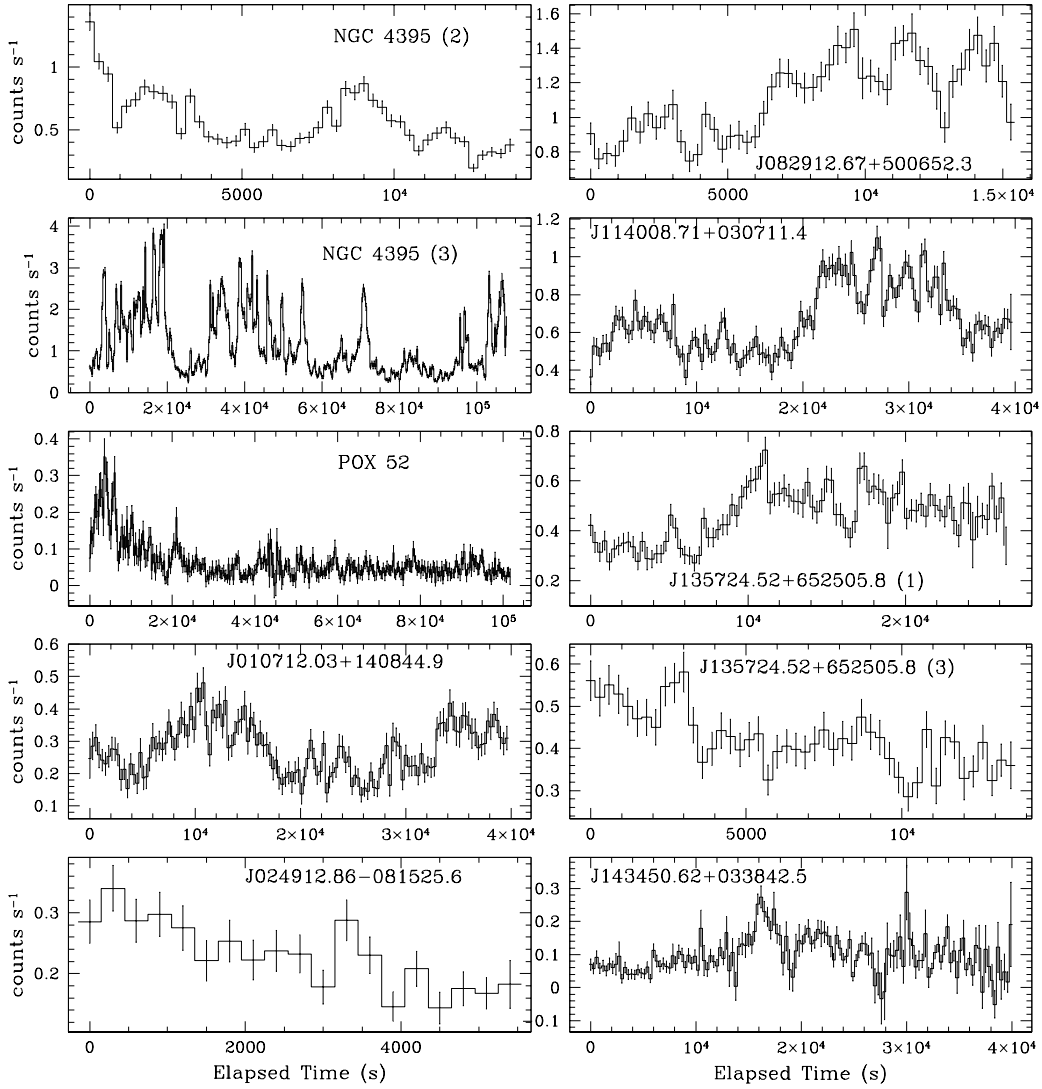


FIG. 1.— *XMM-Newton* X-ray lightcurves of AGNs with IMBH derived from the EPIC-pn data with 300 s bins.

TABLE 3
GENERAL PROPERTIES OF THE EPIC-PN LIGHTCURVES OF AGNs WITH IMBH

Object	Data	Bin size (s)	Number of bins	mean rate (count s ⁻¹)	rms	Excess variance (σ_{XS}^2)	Normalized Excess variance (σ_{NXS}^2)	F_{var} (%)
NGC 4395	(2)	300	47	0.57 ± 0.047	0.22 ± 0.045	0.05 ± 0.02	0.15 ± 0.06	39.0 ± 7.8
	(3)	300	360	1.17 ± 0.071	0.77 ± 0.057	0.59 ± 0.088	0.43 ± 0.053	65.6 ± 4.0
POX 52	(1)	300	340	0.06 ± 0.02	0.05 ± 0.012	0.002 ± 0.001	0.54 ± 0.14	73.6 ± 9.3
J010712.03+140844.9	(1)	300	133	0.27 ± 0.036	0.07 ± 0.02	0.005 ± 0.003	0.06 ± 0.04	24.7 ± 7.5
J024912.86-081525.6	(1)	300	19	0.23 ± 0.03	0.04 ± 0.03	0.002 ± 0.002	0.04 ± 0.05	19.7 ± 12.7
J082912.67+500652.3	(3)	300	52	1.11 ± 0.08	0.21 ± 0.08	0.04 ± 0.033	0.03 ± 0.02	18.6 ± 7.2
	(1)	300	133	0.67 ± 0.05	0.16 ± 0.04	0.03 ± 0.013	0.06 ± 0.03	24.4 ± 5.8
J135724.52+652505.8	(1)	300	89	0.46 ± 0.05	0.09 ± 0.03	0.009 ± 0.007	0.04 ± 0.03	20.5 ± 7.4
	(3)	300	46	0.42 ± 0.04	0.06 ± 0.03	0.003 ± 0.004	0.02 ± 0.02	13.9 ± 8.4
J143450.62+033842.5	(1)	300	134	0.10 ± 0.04	0.04 ± 0.02	0.002 ± 0.001	0.20 ± 0.11	44.6 ± 13.0

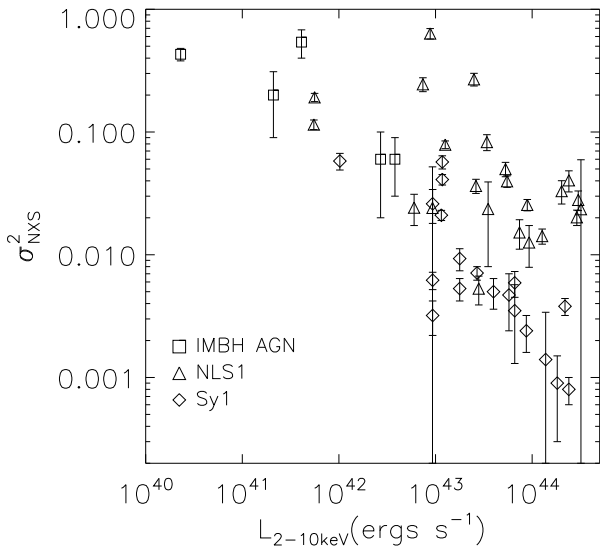


FIG. 2.— Normalized excess variance and 2–10 keV X-ray luminosity for AGNs with IMBH, NLS1 galaxies (Leighly 1999a) and Seyfert 1 galaxies (Nandra et al. 1997)

we did not find systematic *XMM-Newton* study of samples of NLS1s and BLS1s, similar to that performed by Leighly (1999a) and Nandra et al. (1997). Therefore, we used results from Leighly (1999a) for NLS1 and Nandra et al. (1997) for BLS1s with the exclusion of two NLS1s NGC 4051 and Mrk 335. In Figure 2, we have plotted the normalized excess variance as a function of 2–10 keV luminosity for AGNs with IMBHs, NLS1s and BLS1s. As pointed out by Papadakis & Lawrence (1993) and Leighly (1999a), the normalized excess variance depends on the length of observation. The normalized excess variance is the integration of the power density spectrum over a certain frequency range implied by the bin size and the length of the observation. The rednoise nature of the AGN variability means a strong dependence of excess variance on the length of the observation. Therefore, care must be taken in interpreting Fig. 2. Some of AGNs with IMBH were observed for a short duration. To minimize the effect of observation length, we have plotted only those five AGNs with IMBHs that were observed for at least 30 ks, thus making the length of observations similar to that for the NLS1s in Leighly (1999a) and BLS1s in Nandra et al. (1997). The prototype of AGNs with IMBH NGC 4395 lies at the low luminosity end in Fig. 2. The excess variance of NGC 4395 is comparable to some of the most variable NLS1s. Vaughan et al. (2005) have noted that the variations in the soft X-ray emission from NGC 4395 are among the most violent seen in an AGN to date, with the fractional variability amplitude exceeding 100%. Previously, Nandra et al. (1997) and Leighly (1999a) have noted that the excess variance is inversely correlated with the X-ray luminosity though with a flat-

ter slope of ~ -0.3 for NLS1s compared with the slope of ~ -1 for BLS1s. The five AGNs with IMBHs follow the general trend of anticorrelation between σ^2 and L_{2-10} keV of Seyfert galaxies. While three of them follow the anticorrelation for BLS1, one (POX 52) is clearly in the NLS1 zone while NGC 4395 lies below the extrapolation of the BLS1 trend.

3.1. Power density spectra

Only two AGNs, NGC 4395 and POX 52, were observed with long ~ 100 ks exposures that allow us to probe power density spectra (PDS) over a broad range of frequency. Vaughan et al. (2005) have already derived the PDS of NGC 4395 using the long observation that showed a clear break from a flat spectrum ($\alpha \sim 1$) to a steeper spectrum ($\alpha \sim 2$) at a frequency $0.5-3.0 \times 10^{-3}$ Hz. Here we present the PDS for POX 52.

To derive the PDS, we re-extracted the source and background lightcurves for POX 52 with time bins of 500 s. Figure 1 shows the background corrected EPIC-pn lightcurve of POX 52. Fig. 3 also shows the EPIC-pn background level relative to the net source level. The background rate varied in the first 15 ks of observation and then it was steady except for the a flare near the elapsed time of ~ 45000 s. We calculated a power density spectrum (PDS) using the background corrected EPIC-pn light curves sampled at 500 s. For this purpose, we excluded the first 15 ks exposure to minimize the effect of varying background. We used the ‘powspec’ program in XRONOS. We rebinned the PDS in logarithmic space with a binsize of 4 and performed the fitting within the ISIS (version 1.4.8) spectral fitting environment. The PDS is shown in Figure 4 (*left panel*). The power arising from the Poisson errors has not been subtracted. The Poisson errors dominate the PDS above a frequency of $\sim 4 \times 10^{-4}$ Hz. A simple power-law (Power $\propto f^{-\alpha}$) and a constant model resulted in a minimum $\chi^2 = 15.6$ for 23 degrees of freedom (dof) with $\alpha = 1.6 \pm 0.3$. The constant power was fixed to the value expected from the noise. There is a weak excess of power at a frequency of $\sim 3 \times 10^{-4}$ Hz that is reminiscent of quasi-periodic oscillations (QPO). However, neither the QPO-like feature nor a break in the PDS is statistically significant. Hence we conclude that the PDS of POX 52 is consistent with a simple power law and the determination of a break or the QPO-like feature will require future high signal-to-noise long X-ray observations. The non-detection of a break may be due to the dominance of the Poisson noise and the QPO-like feature above a frequency of $\sim 2 \times 10^{-4}$ Hz below which the high frequency break is likely to be present.

J1140+0307 is another AGN in our sample that has good signal-to-noise, ~ 40 ks long X-ray lightcurve. We have derived the PDS of J1140+0307 using the EPIC-pn data. First we extracted a lightcurve with 7.34 s bins. The source lightcurve was corrected for background contribution though the background rate was stable throughout the observation. As before we calculated the PDS and rebinned logarithmically into bins of sizes 15. A simple power-law plus constant model provided a minimum $\chi^2 = 213$ for 177 dof with power-law index steeper than 1.26. Using a broken power-law model in place of the simple power-law improved the fit. However,

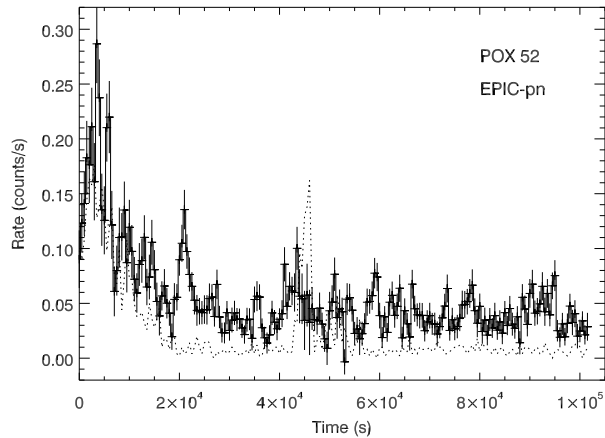


FIG. 3.— The background subtracted EPIC-pn lightcurve of PoX 52 with 500 s bins and in the energy band of 0.2 – 10 keV. Also shown is the background level as dotted line in the same energy band.

TABLE 4

BEST-FIT PARAMETERS FOR THE POWER DENSITY SPECTRUM OF POX 52 & J1140+0307

Model	Parameter	POX 52	J1140+0307
Power law	α	1.6 ± 0.3	> 1.26
Constant	C	30.0 (fixed)	1.7 ± 0.1
	χ^2/dof	15.6/23	213/177
Broken power-law	α_1	–	$1.0^{+0.8}_{-0.9}$
	α_2	–	3 (fixed)
	f_{br} (Hz)	–	$0.7^{+1.2}_{-0.5} \times 10^{-3}$
Constant	C	–	$1.70^{+0.07}_{-0.08}$
	χ^2/dof	–	203.6/176

all the parameters were not well constrained. We needed to fix the power-law index α_2 after the break at its best-fit value to calculate the errors. This procedure resulted in $\chi^2/dof = 203.6/176$. The break frequency is in the range $(0.2 - 1.9) \times 10^{-3}$ Hz, index $\alpha_1 = 0.1 - 1.8$, while the α_2 was fixed at 3. Figure 4 (*right panel*) compares the PDS, the power-law model (dashed line) and the broken power-law model (solid line). Table 4 lists the PDS fit parameters. The broken power-law model is an improved fit over the simple power-law model at a confidence level of 99.5%, thus the departure from the simple power-law is likely real. However, a long *XMM-Newton* observation is required to measure the break frequency reliably.

4. SPECTRAL ANALYSIS

We have performed spectral analysis of the eight AGNs with IMBH. We present the results based on the EPIC-pn data only as these data have the highest signal-to-noise. The spectra were analyzed with the Interactive Spectral Interpretation System (ISIS, version 1.4.8). The errors on the best-fit spectral parameters are quoted at 90% confidence level.

4.1. NGC 4395

We begin our spectral analysis with the high signal-to-noise spectrum of NGC 4395 obtained on 2003 November 30. We grouped the EPIC-pn data to a minimum of 100 counts per spectral channel and fitted a simple power-law (PL) model absorbed by the Galactic column

to the 0.3–10 keV spectrum. This model provided unacceptable fit ($\chi^2/dof = 5627.7/485$). The observed data, the absorbed PL model and the deviations are shown in the upper left panel of Figure 5. Evidently the X-ray emission from NGC 4395 is complex, showing evidence for emission/absorption features below 2 keV and narrow iron $K\alpha$ line at ~ 6.4 keV. The lack of emission near 1 keV and slight curvature in the 1–10 keV band clearly suggest the presence of neutral/warm absorber covering the primary source of X-ray emission fully or partially.

As a next step, we added a partially covering neutral absorber component (*zpcfabs*) to the PL model and performed the fitting to the 0.3–10 keV data. The addition of the partial covering absorber improved the fit ($\chi^2/dof = 2812.2/483$), though it is still not a good fit. The covering fraction and absorption column suggested by the *zpcfabs* component are ~ 0.8 and $.9 \times 10^{22} \text{ cm}^{-2}$, respectively. The poor quality of the fit is due mostly to the broad emission features at $\sim 0.5 - 0.7$ keV and absorption features at $\sim 0.8 - 1$ keV range. These features arise due to the absorption and emission by warm absorbers.

To investigate the possible presence of a warm absorber medium, we have created a warm absorber model using the spectral simulation code CLOUDY version 7.02.01 (last described by Ferland et al. 1998). We used the ionizing continuum table power-law available within CLOUDY ($f_\nu \propto \nu^\alpha$). We assumed a spectral index of $\alpha = -0.9$ for the spectral range between 10 micron and 50 keV. The continuum has slopes $f_\nu \propto \nu^{5/2}$ at low energies with an infrared break at 10 microns and $f_\nu \propto \nu^{-2}$ at high energies with X-ray break at 50 keV. We also included the cosmic microwave background radiation so that the incident continuum has nonzero intensity at very long wavelengths. We assumed a plane parallel geometry and calculated grids of models by varying the ionization parameter and the total hydrogen column density. We also included UTA features from Gu et al. (2006) in our calculation. The grid of models were imported to ISIS in the form of an XSPEC-style multiplicative table model as described in Porter et al. (2006).

The free parameters of the warm absorber model are absorption column (N_W), ionization parameter ($\log \xi$, where $\xi = L/nr^2$) and the redshift (z). The use of the warm absorber model improved the fit to $\chi^2/dof = 906.9/481$. The remaining features in the residuals of the data and model below 2 keV are broad emission features at ~ 0.6 keV, absorption features at ~ 0.7 keV and ~ 0.9 keV and the lack of emission below 0.4 keV. The features suggest additional warm absorber components. Adding a second warm absorber component further improved the fit to $\chi^2/dof = 854.4/479$. However the absorption feature at ~ 0.7 keV, likely the absorption edge due to O VII, is still not modeled. Adding a third warm absorber component to account for the ~ 0.7 keV absorption feature improved the fit to $\chi^2/dof = 754.2/477$. Examination of the residuals shows a lack of emission below ~ 0.4 keV suggesting additional neutral absorption. We have kept fixed the neutral column at the Galactic value in all the above fits. Adding a neutral absorber component in addition to the Galactic column improved the fit to $\chi^2/dof = 548.3/476$. Finally, addition of a

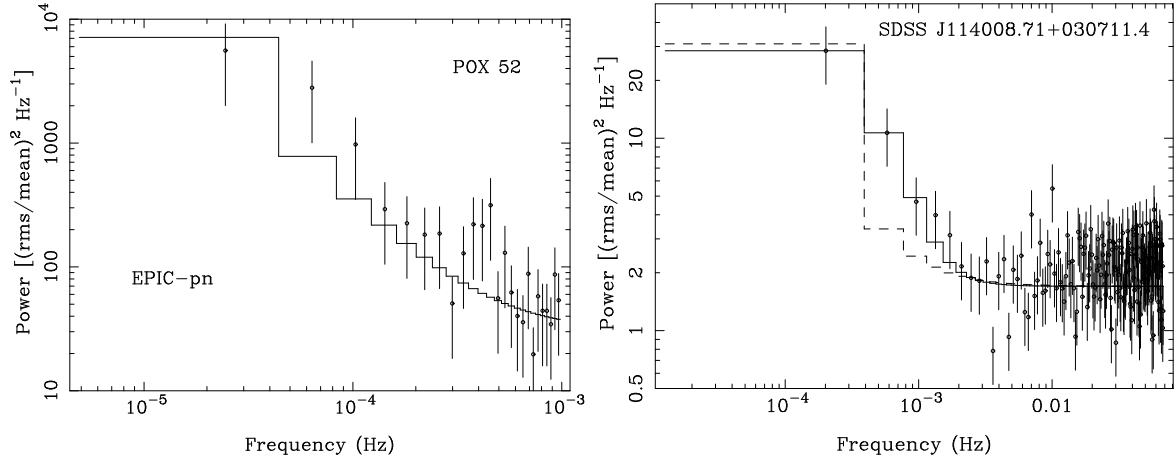


FIG. 4.— *Left*: Power density spectrum of Pox 52 derived from the full band EPIC-pn lightcurve after excluding the first 15 ks exposure to minimized the effect of varying background. *Right*: Power density spectrum of J1140+0307 and the best-fit models – a broken power law plus a constant (solid line) and a simple powerlaw plus a constant (dashed line).

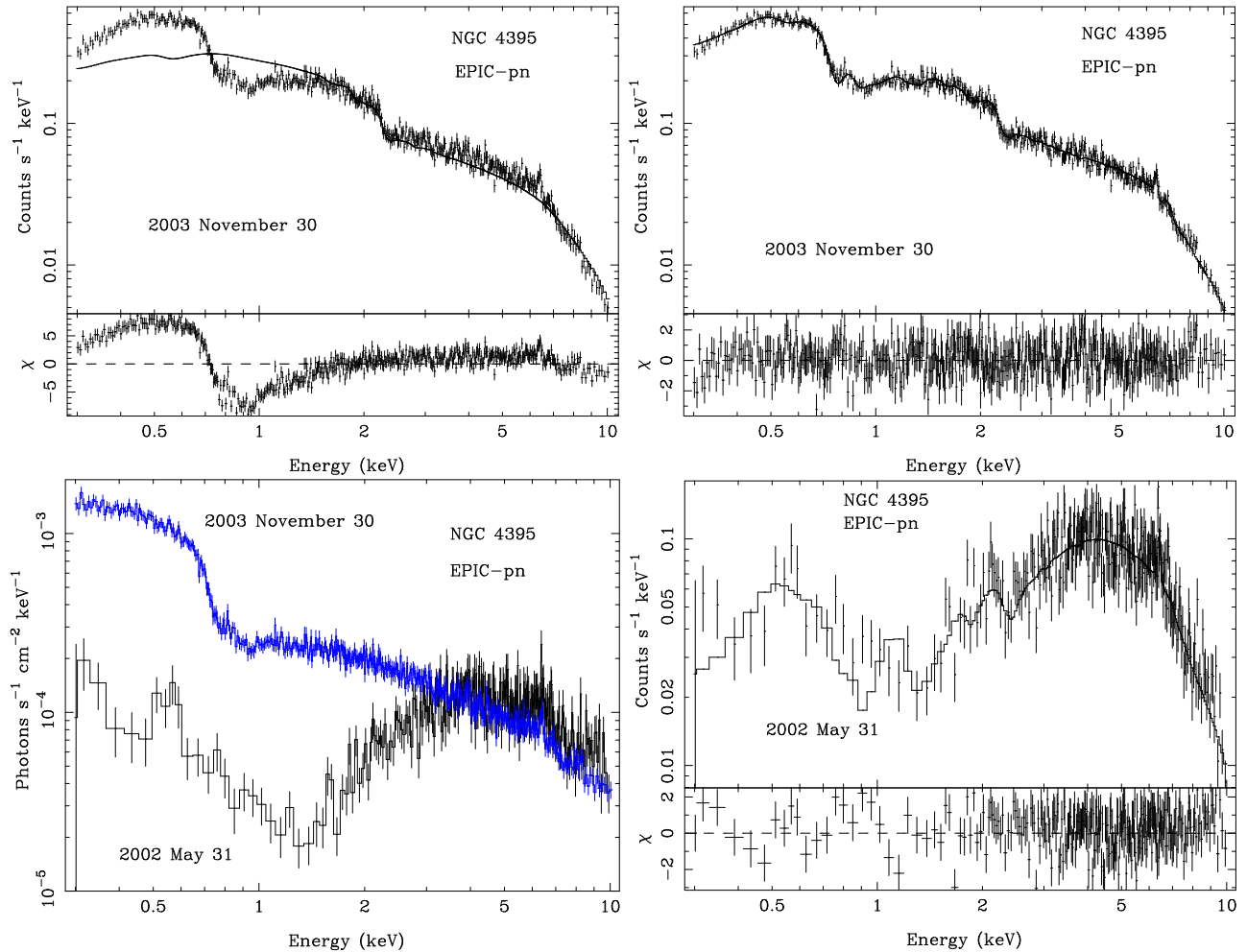


FIG. 5.— Results of the spectral analysis of NGC 4395. *Upper left*: EPIC-pn data obtained in 2003 November 30, the absorbed power-law model and the deviations. *Upper right*: EPIC-pn data of 2003 November 30, the best-fit model consisting of a power-law and an iron $K\alpha$ line, modified by the Galactic absorption, intrinsic neutral and warm absorbers. *Lower left*: A comparison of unfolded EPIC-pn spectra of NGC 4395 obtained on 2003 November 30 and 2002 May 31. *Lower right*: EPIC-pn data of 2002 May 31, the best-fit model and the deviations.

TABLE 5
PARAMETERS FOR NGC 4395 AND POX 52 OBTAINED FROM THE BEST-FITTING MODELS TO THE EPIC-PN DATA.

Component	Parameter ¹	2003 November	NGC 4395 2003 January 3	2002 May 31	POX 52 2005 July 8
Gal. Abs.	N_H (10^{20} cm ⁻²)	1.85(f)	1.86(f)	1.86(f)	3.85(f)
Excess Abs.	N_H (10^{20} cm ⁻²)	$5.2^{+0.7}_{-0.2}$	5.2(f)	5.2(f)	—
pcfabs	N_H (10^{22} cm ⁻²)	$36.4^{+2.2}_{-3.1}$	$29.2^{+13.0}_{-7.4}$	$8.0^{+2.1}_{-1.2}$	6.2 ± 1.8
	c.f.	$0.49^{+0.0p}_{-0.003}$	$0.44^{+0.08}_{-0.11}$	$0.78^{+0.08}_{-0.15}$	$0.88^{+0.04}_{-0.06}$
WA(1)	N_W (10^{21} cm ⁻²)	$5.8^{+0.1}_{-0.3}$	$5.6^{+1.0}_{-1.2}$	$9.5^{+2.0}_{-2.1}$	$6.3^{+1.8}_{-1.7}$
	$\log\xi$	$2.0^{+0.1}_{-0.2}$	2.2 ± 0.1	2.5 ± 0.1	$1.8^{+0.3}_{-0.8}$
WA(2)	N_W (10^{21} cm ⁻²)	$1.6^{+0.3}_{-0.03}$	$2.5^{+1.4}_{-0.5}$	$5.2^{+1.8}_{-1.1}$	—
	$\log\xi$	$0.0^{+0.0001}_{-0p}$	$0.001^{+0.4}_{-0p}$	$0.009^{+0.4}_{-0p}$	—
WA(3)	N_W (10^{20} cm ⁻²)	$2.6^{+0.1}_{-0.5}$	$1.8^{+0.6}_{-0.8}$	—	—
	$\log\xi$	$3.5^{+0.03}_{-0.05}$	3.7 ± 0.3	—	—
MCD	kT_{in} (eV)	—	—	—	167^{+37}_{-27}
	n_{MCD} ²	—	—	—	$62.9^{+173.8}_{41.1}$
PL	Γ	$1.88^{+0.01}_{-0.02}$	1.88(f)	1.88(f)	2.0 ± 0.3
	n_{PL} ³	$3.5^{+0.02}_{-0.03} \times 10^{-3}$	3.5×10^{-3} (f)	$3.7^{+0.3}_{-0.2} \times 10^{-3}$	$1.7^{+1.2}_{-0.7} \times 10^{-4}$
Gaussian	E (keV)	6.40 ± 0.02	—	6.40(f)	—
	σ (keV)	< 0.05	—	0.01(f)	—
	f_{line} ⁴	$(6.6 \pm 1.7) \times 10^{-6}$	—	$(1.4 \pm 0.5) \times 10^{-5}$	—
Flux	$f_{0.3-2}$ keV ⁵	9.4×10^{-13}	8.4×10^{-13}	1.0×10^{-13}	4.4×10^{-14}
	f_{2-10} keV ⁵	5.5×10^{-12}	5.7×10^{-12}	6.0×10^{-12}	2.7×10^{-13}
	χ^2/dof	508.3/473	286.2/278	323.6/260	209.7/212

¹(f) indicates that the parameter value was fixed. ‘p’ in the upper or lower error value indicates that the upper or lower confidence limit did not converge. ²MCD normalization in units of $n_{MCD} = (R_{in}/\text{km})/(D/10\text{kpc})$, where R_{in} is the inner radius and D is the distance.

³Power-law normalization in units of photons keV⁻¹ cm⁻² s⁻¹ at 1 keV.

⁴Line flux in photons keV⁻¹ cm⁻² s⁻¹.

⁵Observed flux in units of ergs cm⁻² s⁻¹.

narrow Gaussian line for the iron $K\alpha$ line provided an excellent fit ($\chi^2/dof = 508.3/473$). The best-fit photon index is ~ 1.88 . We note that the 5–10 keV spectrum is consistent with an absorber power-law with a photon index $\Gamma \sim 1.84$. Evidently the multiple warm and neutral absorbers strongly modify the spectrum below ~ 5 keV. The parameters of the best-fit model are listed in Table 5 and the observed EPIC-pn spectrum of 2003 November 30, the best-fit model and the deviations are shown in the upper right panel of Fig. 5.

We have also analyzed the EPIC-pn spectrum of NGC 4395 obtained on 2002 May 31 with a net exposure of 12.5 ks. The EPIC-pn data were grouped to a minimum of 20 counts per spectral channel. Fig. 5 (*lower left panel*) shows a comparison of the unfolded EPIC-pn spectra of NGC 4395 obtained on 2002 May 31 and 2003 November 30 in a model independent way. Unlike XSPEC, the unfolded spectrum in ISIS is derived in a model-independent way as follows:

$$f_{unfold}(I) = \frac{[C(I) - B(I)]/\Delta t}{\int R(I, E)A(E)dE}, \quad (1)$$

where $C(I)$ is the number of total counts in the energy bin I , $B(I)$ is the number of background counts, Δt is exposure time, $R(I, E)$ is the normalized response matrix and $A(E)$ is the effective area at energy E . This definition produces a spectrum that is independent of fitted model. It is clear from Figure 5 that the X-ray spectrum of NGC 4395 varied drastically below ~ 3 keV but remained similar at harder energies. The presence of the dip near 1 keV in the spectrum of 2002 May clearly suggests heavy obscuration by neutral or partially ionized material. Thus we expect that the best-fit model inferred from 2003 November observation should also be appropriate for 2002 May observation except for different absorption columns of either neutral or warm absorber components. Thus we fit the model of 2003 November observation to the EPIC-pn data obtained on 2002 May with the parameters fixed at their best-fit values and we varied the parameters of the absorbing components. First we varied the parameters of the partial covering absorption model and then those of the warm absorber components as required to obtain a good fit. We additionally needed to vary the normalizations of the power law and the narrow Gaussian line at 6.4 keV. The warm absorber model with the highest ionization parameter for the 2003 November data was not required for the 2002 May data. The fully covering intrinsic neutral absorption did not vary. The best-fit parameters for the 2002 May data are listed in Table 5 and the observed data, the best-fit model and the deviations are shown in the lower right panel of Fig. 5. As expected, the covering fraction was higher ($\sim 80\%$) in 2002 May, compared to $\sim 50\%$ in 2003 November. As seen in Table 5, most of the spectral variability is caused by the change in the partial covering and warm absorbers.

The model for the 2003 November data also describes the EPIC-pn data obtained on 2003 Jan 3 except for small changes in the parameters of the partial covering and warm absorber components (see Table 5). An iron $K\alpha$ line was not detected in the observation of 2003 Jan 3. The model provided $\chi^2/dof = 286.2/278$ with the partially covering absorption model param-

eters $N_H = 2.9_{-0.7}^{+1.3} \times 10^{23}$ cm $^{-2}$ and covering fraction of $44_{-11}^{+8}\%$. Thus the covering fraction was $\sim 80\%$ in 2002 May, $\sim 50\%$ in 2003 Jan and 2003 November.

The best-fit model for the 2003 November data suggests absence of soft X-ray excess emission below 2 keV that is observed from many NLS1 galaxies. We have estimated an upper-limit to the strength of the soft X-ray excess emission. First we fitted a simple absorbed power-law model to the 5–10 keV data in order to minimize the effect of multiple absorber components on the intrinsic spectral shape and obtained $\Gamma_{5-10 \text{ keV}} = 1.84$. To estimate the upper-limit to the soft excess emission, we added a multicolor disk blackbody component (MCD) to the best-fit model to the 2003 November data and fixed the photon index to $\Gamma = \Gamma_{5-10 \text{ keV}}$ and calculated the upper-limit to the flux of the MCD component. We obtained an upper-limit of 22% for the strength of the soft excess emission relative to the PL component in the 0.3–2 keV band.

4.2. POX 52

The EPIC-pn spectrum of POX 52 was grouped to a minimum of 20 counts per spectral channel. First we fitted a simple absorbed PL model to the pn data in the 0.3–10 keV band. This model provided an unacceptable fit ($\chi^2/dof = 1004.5/217$). We have plotted the observed data, the power-law model and the χ residuals in Figure 6 (*left panel*). The deviations of the data from the PL model clearly show a soft X-ray excess emission below 0.7 keV and a broad hump in the 2.5–7 keV band. The deviations are qualitatively similar to that for NGC 4395 albeit with reduced strength of soft excess and no iron $K\alpha$ line (see Fig. 5, upper left panel). Adding a partial covering neutral absorber to the PL model improved the fit ($\chi^2/dof = 429.8/216$) but the fit is not acceptable. The residuals showed absorption features at energies $\sim 0.7 - 1.1$ keV, suggestive of the presence of warm absorber medium. We used the same warm absorber model created earlier for NGC 4395 to fit the EPIC-pn spectrum of POX 52 (see Section 4.1). The addition of the warm absorber model to the PL model modified by a partial covering neutral absorber improved the fit, providing an excellent fit ($\chi^2/dof = 212.2/214$). The best-fit photon index is steep ($\Gamma = 2.4 \pm 0.2$). However, a simple absorbed power-law model fit to the 5–10 keV band data provided $\Gamma = 2.0_{-0.4}^{+0.6}$. The discrepancy is most likely due to the presence of multiple absorbers as it is difficult to infer the intrinsic spectral shape if most of the observed band is strongly affected by absorbers. Therefore, we fixed $\Gamma = 2.0$ in our best-fit model to the full band spectrum and performed the fitting. The fit worsened to $\chi^2/dof = 230.5/215$. The residuals suggested possible presence for a soft X-ray excess component. Addition of a multicolor disk blackbody (MCD) model and varying the photon index improved the fit to $\chi^2/dof = 209.7/212$. The best-fit photon index is $\Gamma = 2.0 \pm 0.3$ similar to that obtained for the 5–10 keV band data. The EPIC-pn data, the best-fit model and the deviations are plotted in Fig. 6 (see right panel). The best-fit parameters are listed in Table 5. In the 0.3–2 keV band, the soft X-ray excess and the power-law component have similar fluxes.

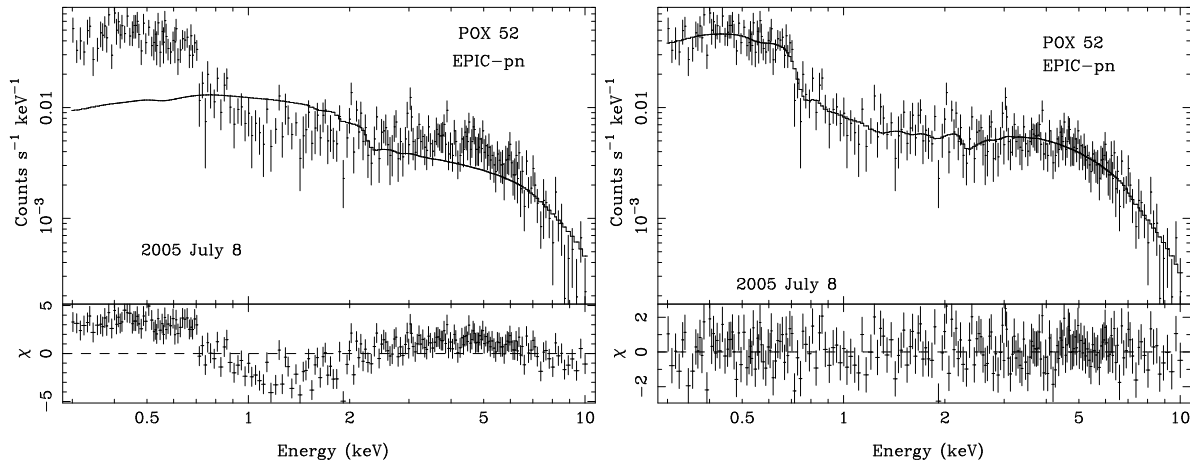


FIG. 6.— *Left*: Observed EPIC-pn spectrum, absorbed power-law model and the deviations. *Right*: Observed EPIC-pn spectrum, the best-fit model consisting of a power law and an MCD modified by a multiple absorbing components – the Galactic, partially covering neutral absorption and a warm absorber. Also shown are the deviations of the observed data from the best-fit model.

4.3. SDSS AGNs with IMBH

There are seven observations of six SDSS AGNs with IMBHs that are suitable for spectral fitting. All the EPIC-pn spectra were grouped to a minimum of 20 counts per spectral channel. These spectra are relatively simple compared to that of NGC 4395 or POX 52. As a first step, we fitted a simple power-law modified with Galactic absorption to the individual spectra. The residuals of the observed data from the power-law model showed evidence for weak soft excess emission in the case of J0249-0815, J1140+0307 and J1357+6525. Addition of a multicolor disk blackbody component to the PL model improved the fit marginally for J0249-0815 only at a level of 97.4% ($\Delta\chi^2 = -8.5$ for two additional parameters) based on the f-test. The best-fit parameters are $kT_{in} = 169_{-50}^{+43}$ eV and $\Gamma = 1.72 \pm 0.30$. For J1140+0307, the addition of the MCD component provided significant improvement over the power-law model ($\Delta\chi^2 = -64.6$ for one additional parameter). Varying the absorption column did not improve the fit further. The best-fit parameters are $kT_{in} = 181_{-7}^{+3}$ eV and $\Gamma = 2.4 \pm 0.1$. J1357+6525 has two observations. Both data show evidence for weak soft excess emission. The spectral shapes are similar withing errors for both the observations except for a narrow iron $K\alpha$ line at 6.65 keV which has been detected in the first observation at a level of 99.3% based on the F-test. The best-fit parameters for the SDSS AGNs are listed in Table 6.

The simple power-law model provided statistically acceptable fits to the pn data of J0107+1408, J0829+5006 and J1434+0338 with photon indices $\Gamma = 2.4 \pm 0.1$, 2.65 ± 0.08 , 2.05 ± 0.07 , respectively. The steep photon indices suggest possible presence of the soft X-ray excess emission from these AGNs. However, addition of an MCD component did not improve any of the fits statistically at 95% level. To further investigate the presence of the soft excess component, we fitted the absorbed power-law model only to the hard 2.5 – 10 keV and found generally flatter indices. To estimate the strength of the soft excess emission from these AGNs, we added MCD components to the power-law model and fixed the power-law index to the best-fit values obtained for the 2.5 – 10 keV data. The fit qualities are similar to the simple power-

law fits. Thus the data are consistent with the presence of the soft excess but do not require this component statistically. Therefore, we calculated 90% upper-limits to the strength of the soft excess emission. The upper limits are listed in Table 7. In Figure 7, we show the strength of the soft X-ray excess from the SDSS AGNs with IMBHs as the ratios of the observed data and the best-fit 2.5 – 10 keV power-law model extrapolated to lower energies. For comparison, we have also plotted the ratios for NGC 4395 and POX based on the best-fit absorbed power law to the 5 – 10 keV data as the X-ray emission below ~ 5 keV is strongly modified by the intrinsic neutral and warm absorber.

5. UV EMISSION AND OPTICAL-TO-X-RAY SPECTRAL INDEX

An additional advantage of *XMM-Newton* is the availability of the OM that provides optical/UV data simultaneously with the X-ray observations. All AGNs with IMBHs were observed with the OM in the imaging mode with one or more optical/UV filters. The AGNs were observed in the UV for the first time, therefore we provide here standard UV magnitudes and fluxes based on the OM observations. The OM data were processed using the SAS task *omichain*. In all cases, multiple exposures were taken in the same filter and the standard magnitudes and flux densities were derived based on the average count rates (Cohen 2004). We list the average count rates, standard magnitude and flux densities for each of the observations in Table 8. We corrected the flux densities for the Galactic extinction by adopting the extinction law in Cardelli et al. (1989). We calculated the color excesses $E(B-V)$ due to the Galactic reddening from the Galactic hydrogen column density (N_H) along the lines of sight to individual AGNs using the relation

$$N_H = 5.8 \times 10^{21} \times E(B - V) \text{ cm}^{-2} \quad (2)$$

(Bohlin et al. 1978). The unreddened flux densities are listed in Table 8.

We have also calculated the optical-to-X-ray spectral index (α_{ox}) defined as

$$\alpha_{ox} = -0.386 \log \left(\frac{L_\nu(2500\text{\AA})}{L_\nu(2 \text{ keV})} \right) \quad (3)$$

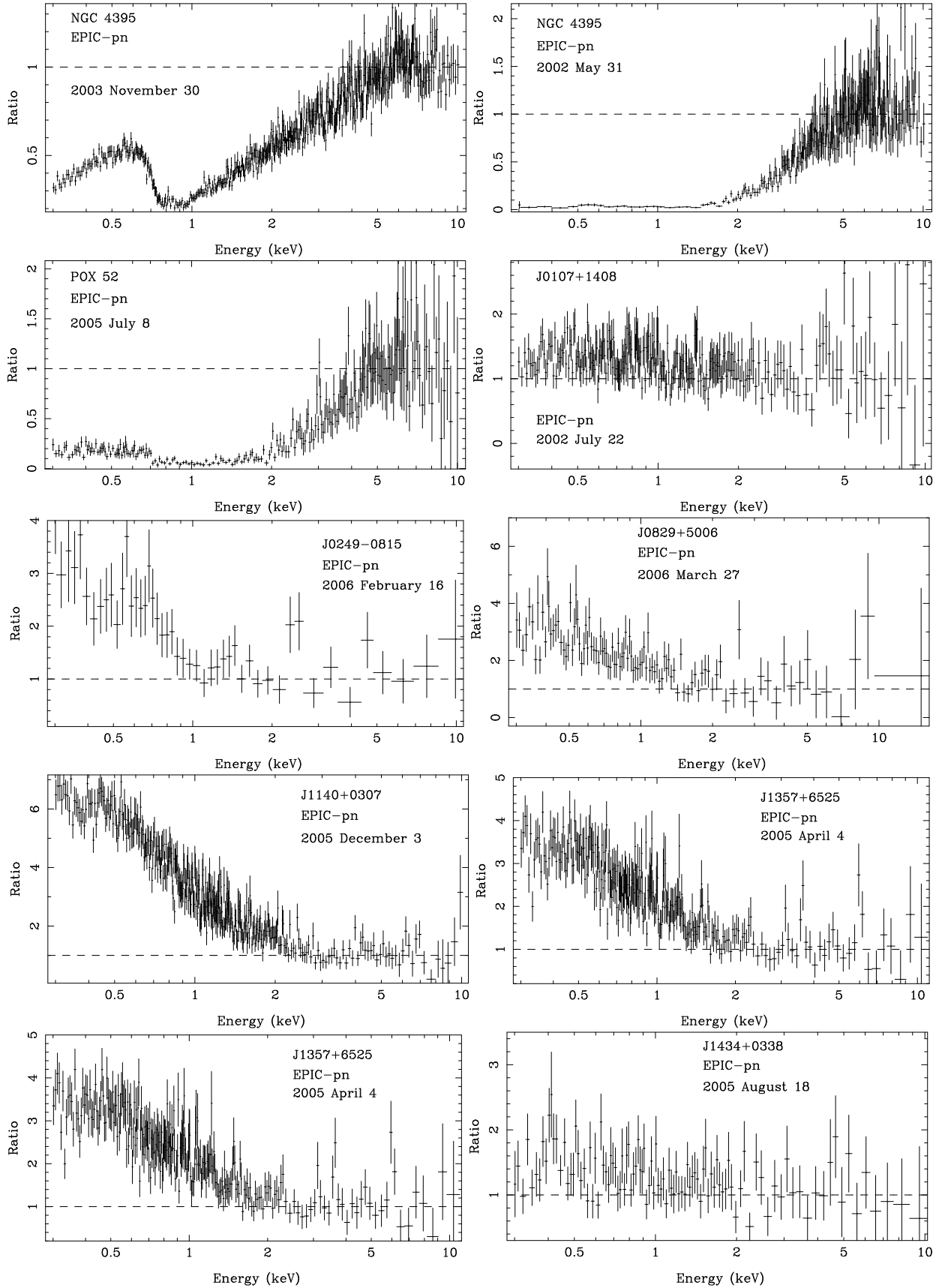


FIG. 7.— The ratios of EPIC-pn data and the best-fitting power-law model modified by the line of sight Galactic absorption. The power law was fitted to 2.5 – 10 keV data for the IMBH AGNs discovered with the SDSS and extrapolated to lower energies to calculate the ratios. For NGC 4395 and POX 52, the ratios were obtained by fitting the absorbed power law to the 5 – 10 keV band as the primary continua of the two AGNs are strongly modified below 5 keV by the multiple absorbing components.

TABLE 6
THE BEST-FITTING SPECTRAL PARAMETERS FOR SDSS AGNs.

Object	Data	Model	Cold N_H (10^{20} cm^{-2})	kT_{in}	Γ	$(E_{FeK\alpha}, \sigma, f_{FeK\alpha}^1)$ (keV), (keV),	f_{soft}^2	f_{hard}^2	χ^2/dof
J0107+1408	(1)	PL	4.5 ± 1.0	–	2.4 ± 0.1	–	3.4	1.9	213.1/236
		PL+MCD	$5.1^{+2.0}_{-1.6}$	157^{+49}_{-28}	2.20(f)	–	3.3	2.2	209.9/235
J0249–0815	(1)	PL	3.67(f)	–	$2.2^{+0.2}_{-0.1}$	–	3.4	2.5	52.4/46
		MCD+PL	3.67(f)	169^{+33}_{-41}	1.6 ± 0.3	–	3.2	4.1	37.9/44
J0829+5006	(3)	PL	4.08(f)	–	2.64 ± 0.08	–	12.2	4.5	102.4/101
		PL+MCD	4.08(f)	181^{+23}_{-22}	2.04(f)	–	11.8	6.6	100.6/100
J1140+0307	(1)	PL	3.9 ± 0.6	–	2.93 ± 0.06	–	7.8	1.8	424.2/333
		MCD+PL	1.91(f)	181^{+8}_{-7}	$2.40^{+0.08}_{-0.09}$	–	7.7	2.4	359.6/332
J1357+6525	(1)	PL	$2.4^{+0.90}_{-0.85}$	–	2.60 ± 0.08	–	5.4	1.9	287.5/237
		MCD+PL	1.36(f)	184 ± 16	2.18 ± 0.13	–	5.3	2.5	266.8/236
	(3)	MCD+PL+GL	1.36(f)	186^{+18}_{-17}	2.23 ± 0.13	$6.65^{+0.05}_{-0.10}, 0.01(\text{f}), 1.7 \pm 0.9$	5.4	2.5	255.6/234
		PL	$2.1^{+1.1}_{-1.0}$	–	2.5 ± 0.1	–	5.0	2.2	207.7/160
J1434+0338	(1)	MCD+PL	1.36(f)	186^{+16}_{-17}	1.93 ± 0.15	–	4.9	3.0	176.8/160
		PL	2.43(f)	–	2.05 ± 0.07	–	1.3	1.2	101.0/103
		PL+MCD	2.43(f)	208^{+89}_{-80}	1.86(f)	–	1.3	1.3	101.3/102

¹Iron line flux in units of $10^{-6} \text{ photons cm}^{-2} \text{ s}^{-1}$.

² f_{soft} and f_{hard} are flux in the soft (0.3 – 2 keV) and hard (2 – 10 keV) bands in units of $10^{-13} \text{ ergs cm}^{-2} \text{ s}^{-1}$.

TABLE 7
STRENGTH OF SOFT X-RAY EXCESS EMISSION, LUMINOSITY & ACCRETION RATES FOR AGNs WITH IMBHs.

Object	$\frac{L_{MCD}}{L_{PL}}$ (0.3 – 2 keV)	$\frac{L_{MCD}}{L_{PL}}$ (0.6 – 10 keV)	$L(0.3 – 10 \text{ keV})$ (ergs s^{-1})	$L(2 – 10 \text{ keV})$ (ergs s^{-1})	$\frac{L_X}{L_{Edd}}$
NGC 4395	< 0.22	< 0.02	4.5×10^{40}	2.3×10^{40}	1.0×10^{-3}
POX 52	1.0	0.24	1.4×10^{42}	4.1×10^{41}	0.07
J0107+1408	< 0.28	< 0.08	9.2×10^{42}	2.7×10^{42}	0.11
J0249–0815	0.80	0.11	1.6×10^{42}	8.4×10^{41}	0.11
J0829+5006	< 1.6	< 0.4	9.1×10^{42}	1.9×10^{42}	0.14
J1140+0307	0.61	0.24	1.8×10^{43}	3.8×10^{42}	0.24
J1357+6525	0.42	0.14	2.3×10^{43}	6.6×10^{42}	0.19
J1434+0338	< 1.9	< 0.5	4.8×10^{41}	2.1×10^{41}	0.02

where $L_\nu(2500\text{\AA})$ and $L_\nu(2\text{ keV})$ are the intrinsic luminosity densities at 2500\AA and 2 keV , respectively. We have derived the flux densities from the OM and EPIC-pn observations. NGC 4395 was observed in four filters UVW1, UVW2, U and B during the third observation, we calculated the flux density at 2500\AA by fitting a power-law $f_\nu \propto \nu^{\alpha_{UV}}$ to the unreddened OM flux densities. For other AGNs with flux densities available in two OM filters, we calculated $f_\lambda(2500\text{\AA})$ by directly calculating α_{UV} and the normalization of the power law. For POX 52, J0249-0815 and J1434+0338 with flux densities available in single UV filter, we assumed a UV spectral index, $\alpha_{UV} = -0.9$, the same as that derived for NGC 4395. The UV spectral indices and the derived monochromatic fluxes at 2500\AA are listed in table 9. The flux densities at 2 keV were derived from the best-fit models to the EPIC-pn data obtained simultaneously with the OM data and were corrected for the Galactic and any neutral or warm absorption. The flux densities at 2 keV are also listed in Table 9 along with the α_{ox} values.

6. DISCUSSION

We have examined X-ray/UV properties of eight AGNs with IMBHs using 12 *XMM-Newton* observations. These constitute the first X-ray study of seven of these AGNs excluding NGC 4395. The primary purpose of this study is to investigate dependence of X-ray spectral and temporal properties on BH mass as these AGNs have the lowest BH masses among all AGNs studied in X-rays to date (see Table 1). All AGNs are strong X-ray/UV sources with $0.3 - 10\text{ keV}$ X-ray luminosities in the range of $4.5 \times 10^{40} - 2.3 \times 10^{43}\text{ ergs s}^{-1}$ and UV luminosity at 2500\AA in the range of $1.1 \times 10^{40} - 3.4 \times 10^{43}\text{ ergs s}^{-1}$.

6.1. X-ray continuum and soft X-ray excess emission

The $0.3 - 10\text{ keV}$ primary X-ray continua of all AGNs with IMBHs consists of either of a single power-law or a soft X-ray excess component and a power-law. Only four AGNs show clear evidence for soft excess emission that is well described by multicolor disk blackbody with $kT_{in} \sim 150 - 200\text{ eV}$. The soft excess emission from the four contribute only *ltsim*50% in the $0.3 - 2\text{ keV}$ band. X-ray spectra of three other AGNs are also consistent with the presence of soft excess emission with similar temperatures but the component is not required statistically. NGC 4395 is the only AGN that clearly lacks strong soft X-ray emission. Figure 8 compares the strength of soft excess and the photon indices of AGNs with IMBHs and NLS1 galaxies studied by Vaughan et al. (1999). The strength of the soft excess emission is shown as the ratio of the soft excess luminosity (L_{excess}) to that of the power-law component (L_{PL}) in the $0.6 - 10\text{ keV}$ band. L_{excess} is the luminosity of the MCD component in case of AGNs with IMBH, while it is the luminosity of the blackbody component for NLS1 galaxies as Vaughan et al. (1999) parameterized the soft excess emission with a blackbody component. We have plotted only the upper limits for the three SDSS AGNs whose X-ray spectra are equally well described by a simple PL or PL+MCD. NLS1s show a large range in the strength of their soft excess emission, contributing $0 - 68\%$ to the $0.6 - 10\text{ keV}$ band, while AGNs with IMBHs appear to show only weak

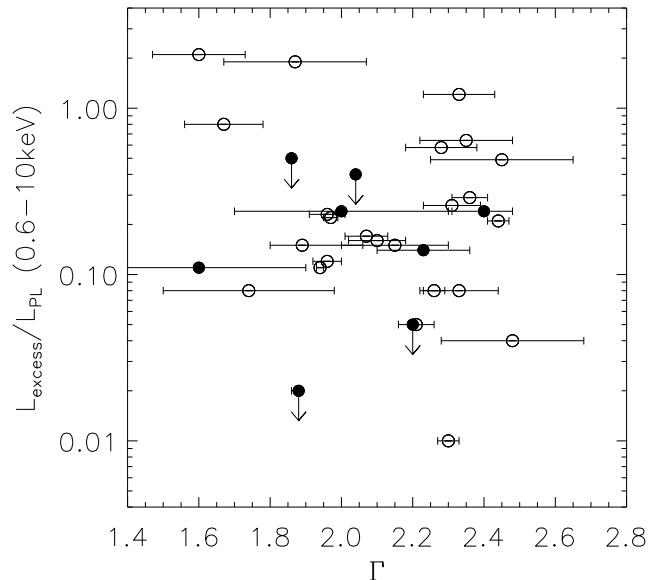


FIG. 8.— Strength of the soft X-ray excess emission in the $0.6 - 10\text{ keV}$ band relative to the power-law in the same band plotted as a function of Γ for AGNs with IMBH (filled circles) and NLS1s (open circles) from Vaughan et al. (1999). The photon indices were derived from the best-fit models with an MCD component for all IMBH AGNs except NGC 4395.

soft excess emission, contributing only $< 35\%$ in the same energy band. NGC 4395 with the lowest L/L_{Edd} has the weakest or no soft excess emission in our sample. Evidently, black hole mass is not the primary driver of the strength of soft X-ray excess emission from AGNs. High L/L_{Edd} is likely the necessary condition for the strong soft X-ray excess emission.

The power-law photon indices of eight AGNs range from $\sim 1.6 - 2.4$ which is similar to that observed from more massive AGNs. In particular, AGNs with IMBHs show similar range in their photon indices as that of NLS1 galaxies (see Fig. 8). The temperature of the soft excess emission detected from the AGNs with IMBHs is also similar to that observed from NLS1 galaxies. In Figure 9, we have plotted kT_{in} and Γ for seven AGNs with IMBHs for which the data are consistent with the presence of soft excess emission. We also show a similar plot in Figure 9 for 19 NLS1 galaxies studied by Vaughan et al. (1999) based on $0.6 - 10\text{ keV}$ *ASCA* data. For NLS1 galaxies and AGNs with IMBHs, the blackbody temperature appears to be uniform in the $100 - 300\text{ eV}$ range irrespective of the photon index.

6.2. X-ray Variability

Strong X-ray variability appears to be a general property of AGNs with IMBH, albeit at different amplitudes. IMBH AGNs are among the most extreme variable radio-quiet AGNs as suggested by the comparison of the normalized excess variances in Fig. 2. The excess variances and X-ray luminosities of AGNs with the smallest black holes are also consistent with the anticorre-

TABLE 8
XMM-Newton OM FLUX MEASUREMENTS

Object	Observation	Filter	Effective wavelength	Count rate ¹ (counts s ⁻¹)	Magnitude ³	f_λ (ergs cm ⁻² s ⁻¹ Å ⁻¹)	
						Reddened	Unreddened
NGC 4395	(2)	UVW1	2905Å	4.0 ± 0.03	17.06 ± 0.01	$(1.9 \pm 0.02) \times 10^{-15}$	$(2.25 \pm 0.02) \times 10^{-15}$
		U	3472Å	9.3 ± 0.06	16.76 ± 0.01	$(1.8 \pm 0.01) \times 10^{-15}$	$(2.08 \pm 0.01) \times 10^{-15}$
	(3)	UVW2	2070Å	0.30 ± 0.007	17.88 ± 0.03	$(1.7 \pm 0.04) \times 10^{-15}$	$(2.24 \pm 0.05) \times 10^{-15}$
		UVW1	2905Å	3.14 ± 0.023	17.32 ± 0.01	$(1.5 \pm 0.01) \times 10^{-15}$	$(1.78 \pm 0.01) \times 10^{-15}$
	(4)	U	3472Å	7.75 ± 0.036	16.97 ± 0.01	$(1.5 \pm 0.01) \times 10^{-15}$	$(1.73 \pm 0.01) \times 10^{-15}$
		B	4334Å	8.07 ± 0.078	16.81 ± 0.01	$(1.0 \pm 0.01) \times 10^{-15}$	$(1.13 \pm 0.01) \times 10^{-15}$
		UVW2	2070Å	0.31 ± 0.015	17.83 ± 0.05	$(1.8 \pm 0.09) \times 10^{-15}$	$(2.38 \pm 0.11) \times 10^{-15}$
		U	3472Å	4.96 ± 0.115	17.45 ± 0.03	$(9.6 \pm 0.22) \times 10^{-16}$	$(1.11 \pm 0.25) \times 10^{-15}$
POX 52	(1)	UVM2	2298Å	0.41 ± 0.004	18.37 ± 0.01	$(9.1 \pm 0.09) \times 10^{-16}$	$(1.56 \pm 0.01) \times 10^{-15}$
J010712+140844	(1)	UVM2	2298Å	0.08 ± 0.005	20.10 ± 0.07	$(1.8 \pm 0.11) \times 10^{-16}$	$(2.92 \pm 0.18) \times 10^{-16}$
		UVW1	2905Å	0.34 ± 0.011	19.72 ± 0.03	$(1.7 \pm 0.054) \times 10^{-16}$	$(2.33 \pm 0.07) \times 10^{-16}$
J024912.86-081525.6	(1)	UVW1	2905Å	0.37 ± 0.023	19.64 ± 0.07	$(1.8 \pm 0.109) \times 10^{-16}$	$(2.52 \pm 0.15) \times 10^{-16}$
J082912.67+500652.3	(1)	UVW1	2905Å	0.91 ± 0.031	18.67 ± 0.04	$(4.4 \pm 0.15) \times 10^{-16}$	$(6.41 \pm 0.22) \times 10^{-16}$
	(3)	UVW1	2905Å	0.93 ± 0.026	18.65 ± 0.03	$(4.5 \pm 0.13) \times 10^{-16}$	$(6.55 \pm 0.20) \times 10^{-16}$
J114008.71+030711.4	(1)	UVM2	2298Å	0.26 ± 0.007	18.87 ± 0.03	$(5.77 \pm 0.15) \times 10^{-16}$	$(7.55 \pm 0.20) \times 10^{-16}$
		UVW1	2905Å	0.73 ± 0.012	18.90 ± 0.02	$(3.53 \pm 0.01) \times 10^{-16}$	$(4.21 \pm 0.02) \times 10^{-16}$
J135724.52+652505.8	(1)	UVM2	2298Å	0.21 ± 0.006	19.08 ± 0.03	$(4.7 \pm 0.13) \times 10^{-16}$	$(5.69 \pm 0.16) \times 10^{-16}$
		UVW1	2905Å	0.69 ± 0.010	18.97 ± 0.02	$(3.3 \pm 0.01) \times 10^{-16}$	$(3.74 \pm 0.01) \times 10^{-16}$
	(2)	UVM2	2298Å	0.21 ± 0.008	19.11 ± 0.04	$(4.6 \pm 0.18) \times 10^{-16}$	$(5.57 \pm 0.22) \times 10^{-16}$
	(3)	UVM2	2298Å	0.19 ± 0.008	19.20 ± 0.04	$(4.2 \pm 0.18) \times 10^{-16}$	$(5.10 \pm 0.22) \times 10^{-16}$
J143450.62+033842.5	(1)	UVM2	2298Å	0.18 ± 0.009	19.26 ± 0.05	$(4.0 \pm 0.20) \times 10^{-16}$	$(5.63 \pm 0.28) \times 10^{-16}$

¹Corrected rate

³UVW1, UVW2, U and B are in AB magnitudes

TABLE 9
 α_{ox} FOR AGNs WITH IMBHs

Object	Observation	α_{UV}	$f_\nu(2500\text{\AA})$	$f_\nu(2\text{ keV})$	$L_\nu(2500\text{\AA})$	$L_\nu(2\text{ keV})$	α_{ox}
			(ergs cm ⁻² s ⁻¹ Hz ⁻¹)	(ergs cm ⁻² s ⁻¹ Hz ⁻¹)	(ergs s ⁻¹ Hz ⁻¹)	(ergs s ⁻¹ Hz ⁻¹)	
NGC 4395	(3)	-0.9	4.1×10^{-27}	1.3×10^{-29}	8.8×10^{24}	2.7×10^{22}	-0.97
POX 52	(1)	-0.9 ^a	3.0×10^{-27}	5.7×10^{-31}	2.9×10^{27}	5.5×10^{23}	-1.44
J0107+1408	(1)	-1.0	5.6×10^{-28}	3.3×10^{-31}	7.9×10^{27}	4.7×10^{24}	-1.24
J0249-0815	(1)	-0.9 ^a	4.1×10^{-28}	3.1×10^{-31}	8.0×10^{26}	6.0×10^{23}	-1.20
J0829+5006	(1)	-0.9 ^a	2.1×10^{-27}	9.2×10^{-31}	9.0×10^{27}	4.0×10^{24}	-1.29
J1140+0307	(1)	-2.5	1.3×10^{-27}	4.1×10^{-31}	2.0×10^{28}	6.6×10^{24}	-1.34
J1357+6525	(1)	-1.8	1.0×10^{-27}	3.7×10^{-31}	2.8×10^{28}	1.0×10^{25}	-1.32
J1434+0338	(1)	-0.9 ^a	9.2×10^{-28}	1.6×10^{-31}	1.6×10^{27}	2.8×10^{23}	-1.45

^aAssumed UV spectral index to calculate the flux at 2500Å.

lation found for BLS1 and NLS1s (Nandra et al. 1997; Leighly 1999a). In Fig. 2, IMBH AGNs and BLS1s seem to form a strong anticorrelation and most of the dispersion in the $\sigma_{NXS}^2 - L_{2-10\text{ keV}}$ relation is caused by the NLS1 galaxies. It is likely that the dispersion in the $\sigma_{NXS}^2 - L_{2-10\text{ keV}}$ relation is due to the variation in the accretion rates ($\dot{m}_E = L_{bol}/L_{Edd}$) as NLS1s have high accretion rates. This trend is indeed expected from the power density spectra. McHardy et al. (2006) have shown a strong correlation between the break frequency, black hole mass and the accretion rate relative to the Eddington rate such that break time scale $T_B \approx M_{BH}^{1.12}/\dot{m}_E^{0.98}$. This implies that at constant black hole mass, the break frequency increases as $\dot{m}_E^{0.98}$, thus increasing the integrated power over certain frequency range covering the high frequency part of the PDS even if the PDS normalization is the same. An increased integrated power also means more excess variance. Thus both the lower

black hole mass and higher accretion lead to higher break frequencies and hence more excess variance, explaining Fig. 2. From optical studies, AGNs with IMBHs show a wide range of L/L_{Edd} (Table1). Accordingly, they also show a range in excess variance, with POX 52, having the highest L/L_{Edd} also showing the highest excess variance.

The power density spectra of NGC 4395, derived by Vaughan et al. (2005), and J1170+0307 are consistent with a flat power-law below a break and steep power-law above the break. The derived break frequencies for IMBH AGNs are the highest observed among all AGNs. The form of the PDS are broadly similar to that of more massive AGNs. In Figure 10, we have plotted the break time scales and black holes masses of the two AGNs with IMBHs along with their massive counterparts. The break frequency and black hole mass for NGC 4395 were taken from Vaughan et al. (2005) and Peterson et al. (2005), respectively. For massive AGNs, the data were taken

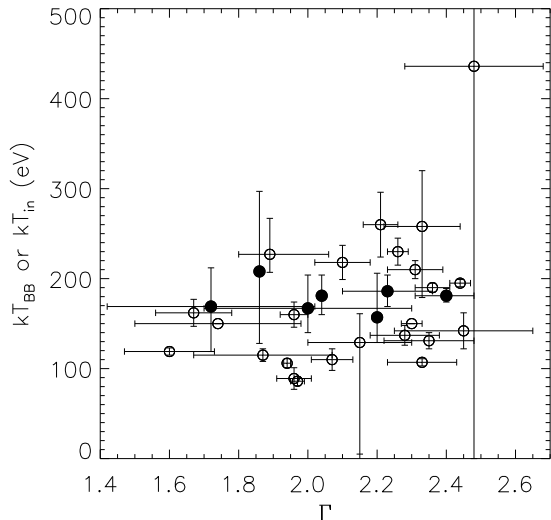


FIG. 9.— Γ Vs MCD kT_{in} for AGNs with IMBHs (filled circles) or blackbody kT_{BB} for NLS1 galaxies (open circles) from Vaughan et al. (1999).

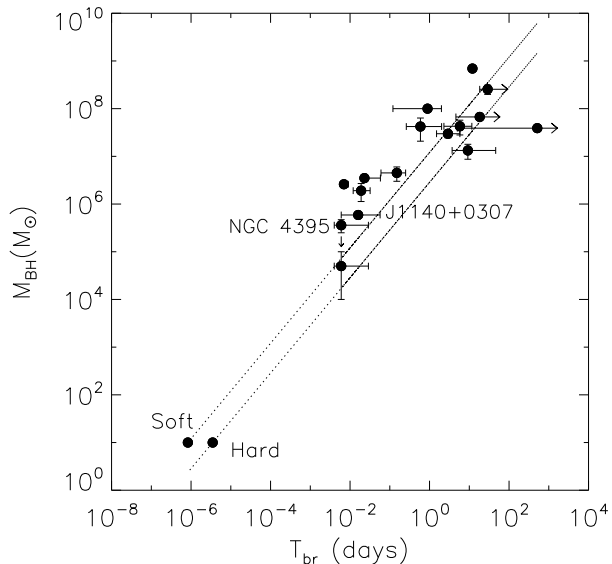


FIG. 10.— The relation between black hole mass and PDS break time scale for AGNs and BHBs. The AGNs with IMBHs, NGC 4395 and J1140+0307 are marked. The dotted lines represent linear scaling, $M_{BH} \propto T_{br}$, based on the typical break times observed from the high/soft (shorter time scales) and low/hard states (longer time scales) of Cyg X-1. See McHardy et al. (2005) for details.

from Uttley & McHardy (2005). The two dotted lines represent assumed linear scaling of black hole mass with break time scale based on the high/soft (shorter time scale at the same black hole mass) and low/hard states of Cyg X-1 (see Uttley & McHardy 2005). The data points located left to the dotted lines represent highly

accreting AGNs. The break time scales and black hole mass of J1140+0307 is consistent with the $M_{BH} - T_{br}$ relation for AGNs and BHBs. However, NGC 4395 with low accretion rate ($\dot{m}_E \simeq 1.2 \times 10^{-3}$; Table 1 and Table 7) is inappropriately placed in Fig. 10. This is due to an order of magnitude uncertainty in the black hole mass of NGC 4395. Filippenko & Ho (2003) argued that the true black hole mass of NGC 4395 is in the range of $10^4 - 10^5 M_{\odot}$ which is consistent with several other measurements (see Vaughan et al. 2005). However, the black hole mass derived from the reverberation mapping by Peterson et al. (2005) is an order of magnitude larger than the best guess value of Filippenko & Ho (2003). When this lower mass of $10^4 - 10^5 M_{\odot}$ is used NGC 4395 data are consistent with other AGNs as was mentioned by Vaughan et al. (2005).

With the $\sigma_{NXS}^2 - L_{2-10keV}$ and $M_{BH} - T_{br}$ relations for IMBH AGNs both being consistent with that for massive AGNs, the variability process of these low mass AGNs are intrinsically the same to that operating in massive AGNs. The extreme variability of AGNs with IMBHs is mainly due to their lower black hole masses.

6.3. $FWHM_{H\beta} - \Gamma_X$ relation

Seyfert 1 galaxies show a large range in the width of their optical permitted emission lines e.g., full width at half maximum (FWHM) of the $H\beta$ line is found to be in the range $\sim 1000 - 10000 \text{ km s}^{-1}$. NLS1 galaxies lie at the lower end of the line width distribution, they were originally identified with $FWHM(H\beta) \lesssim 2000 \text{ km s}^{-1}$ (Osterbrock & Pogge 1985). By this definition, all the AGNs with IMBH qualify as NLS1 galaxies. NLS1 galaxies also show distinct X-ray properties e.g., rapid variability and generally steep X-ray spectrum (Boller et al. 1996; Leighly 1999a,b; Grupe et al. 2004b). NLS1 galaxies show a large dispersion in their soft (0.1 – 2.4 keV) and hard X-ray (2 – 10 keV) photon indices than the BLS1 galaxies with larger $H\beta$ FWHM (Boller et al. 1996; Brandt et al. 1997). The dispersion in the photon indices of IMBH AGNs is similar to that of NLS1 galaxies. The difference is that IMBH AGNs have lower $H\beta$ FWHM on an average than that of NLS1 galaxies. The current best explanation of distinct properties of NLS1 galaxies is that they host low mass black holes that are accreting at high fraction of their Eddington rate. In this picture, the Balmer lines are relatively narrow due to low black hole masses. AGNs with IMBHs play here an important role to investigate if the narrower permitted lines arise solely due to the low black hole mass. In Figure 11, we have plotted the black hole masses as a function of the FWHM of the Balmer lines $H\beta$ or $H\alpha$ line for the AGN with IMBHs. If the black hole mass were the single physical parameter responsible for the width of Balmer's $H\beta$ or $H\alpha$ line, we expect a strong correlation between black hole mass and FWHM of the $H\beta$ or $H\alpha$ line. However, there is no correlation between the two quantities. We have used the reverberation mass for NGC 4395 in Fig 11. As discussed earlier, the measured PDS break frequency for NGC 4395 is consistent with a black hole mass in the range $10^4 - 10^5 M_{\odot}$. However, changing the black hole mass of NGC 4395 in Fig. 11 does not alter our conclusion. In fact, NGC 4395 should have the narrowest $H\beta$ among the AGNs with IMBH if the black hole mass were

the only driving parameter. However, $H\beta$ is broadest for NGC 4395 among the AGNs with IMBHs (see Table 1). Evidently, the black hole mass alone is not responsible for the width of permitted lines.

It is well known from the reverberation mapping of AGNs that the size of the broad line region (BLR) scales with the optical luminosity ($R_{BLR} \propto L^{0.70 \pm 0.03}$; see e.g., Kaspi et al. 2000). Thus, luminosity is another parameter in addition to the black hole mass that determines the width of the permitted lines. This is confirmed in Figure 11, showing that X-ray luminosity relative to the Eddington luminosity is well correlated with the FWHM of the $H\beta$ or $H\alpha$ line. Similar correlation is also observed between the Balmer line widths and Eddington ratio (L_{bol}/L_{Edd}). The anti-correlation between the FWHM of the $H\beta$ line and the X-ray photon index in NLS1s and BLS1s then implies that steep X-ray spectrum is also caused by L/L_{Edd} which is a function of both black hole mass and luminosity. However, we know that the photon index of the X-ray spectrum does not depend on black hole mass as BHBs, massive AGNs and AGNs with IMBHs, all show similar range of photon indices. The photon index, however, depends on the X-ray or bolometric luminosities relative to the Eddington luminosity or the accretion relative to the Eddington rate (see Figure 12). Thus low black hole masses and high absolute accretion rates resulting in high $\dot{m}_E = L_{bol}/L_{Edd}$ are necessary criteria for AGNs to show strong anticorrelation between the $H\beta$ line width and X-ray photon index. Properties of AGNs with low black hole mass and low accretion rates resulting in low \dot{m}_E e.g., NGC 4395, cannot be similar to those of NLS1 galaxies. The accretion processes in the low mass AGNs with low \dot{m}_E are likely similar to the massive AGNs with low \dot{m}_E . This explains the departure of NGC 4395 from the anticorrelation between the FWHM $_{H\beta}$ line and X-ray Γ and similarity with BLS1s in the anticorrelation between normalized excess variance and 2 – 10 keV luminosity. This is indeed consistent with the fact that all NLS1s do not show the steep X-ray spectrum. Dewangan (2002) showed NLS1s with low and high accretion rates relative to the Eddington rate differ in their X-ray characteristics and NLS1s with low \dot{m}_E are similar to the BLS1 galaxies in terms of soft X-ray excess and shape of their X-ray spectra. Based on *Chandra* observations of optically selected, X-ray weak NLS1 galaxies, Williams et al. (2004) showed that strong soft X-ray excess emission and steep X-ray spectrum is not a universal characteristic of NLS1s and many NLS1s have low \dot{m}_E .

6.4. Intrinsic absorption

Among the eight AGNs with IMBHs, NGC 4395 showed the most complex X-ray spectrum. The primary continuum of NGC 4395 observed on 2003 November is modified by multiple absorbers – (i) fully covering neutral absorber ($N_H \sim 5 \times 10^{20} \text{ cm}^{-2}$), (ii) partially covering neutral absorber ($N_H \sim 3.6 \times 10^{23} \text{ cm}^{-2}$ with a covering fraction of $\sim 50\%$), and (iii) three warm absorbers with columns in the range $N_W \sim 0.3 - 5.8 \times 10^{21} \text{ cm}^{-2}$ and ionization parameter $\log\xi \sim 0 - 3.5$). The X-ray spectrum of POX 52 also shows evidence for a partially covering neutral absorber ($N_H \sim 10^{23} \text{ cm}^{-2}$, covering fraction $\sim 90\%$) and warm absorber ($N_W \sim 7 \times 10^{21} \text{ cm}^{-2}$,

$\log\xi \sim 2.1$). The columns and ionization parameters of the warm absorbers in NGC 4395 and POX 52 are well within the range observed for Seyfert 1 galaxies studied by Blustin et al. (2005). Hence the presence of warm absorbers and physical conditions do not depend on black hole mass or accretion rate.

The dramatic spectral variability of NGC 4395 is well accounted by variation in the absorbing components. The covering fraction of the absorber changed from $\sim 80\%$ in 2002 May to $\sim 50\%$ in 2003 November while the absorption column increased in the same period from $N_H = 8_{-1}^{+2} \times 10^{22} \text{ cm}^{-2}$ in 2002 May to $3.6_{-0.3}^{+0.2} \times 10^{23} \text{ cm}^{-2}$ in 2003 November. In addition to the higher covering fraction of the neutral absorber, the warm absorber columns were also higher in 2002 May than 2003 November, though the highly ionized warm absorber was not detected in 2002 May. The decreased covering fraction and warm absorber columns in 2003 November resulted almost an order of magnitude increase in the observed 0.3 – 2 keV flux.

Partial covering of primary X-ray source by cold matter is not uncommon in massive AGNs. The model was first invoked in the early days (Holt et al. 1980). Recently, the partial covering or patchy absorber has been identified in several NLS1 galaxies (Boller et al. 2002; Gallo et al. 2004; Boller 2006; Grupe et al. 2004a, 2007). However, the origin, location, geometry and physical conditions of the partial covering absorbers are not well known. Variations in partial covering absorption has been observed on timescales of weeks to years (Gallo et al. 2004; Grupe et al. 2007). In this respect, NGC 4395 is not unusual except that it is an AGN with low accretion rates. Hence it is unlikely that accretion disk winds act as patchy absorber in NGC 4395 as some models invoke that a partial covering obscuration may arise if our line of sight passes through winds that are launched at intermediate radii of the disk (e.g., Elvis 2000; Proga 2007). In case of NGC 4395, the time scale of variations is long that is apparently not consistent with the toy model of Abrasart & Czerny (2000) suggesting thick clouds at 10 – 100 Schwarzschild radii partially obscure the central source. However, we note that the variability of the partial covering absorption on short time scales, days to weeks, is unknown. Monitoring observations of NGC 4395 with *XMM-Newton* will be very useful to test models for partial covering absorption.

6.5. Broadband continuum properties

One of the great advantages of *XMM-Newton* is the availability of the optical monitor (OM), together with X-ray detectors. As a result, it is possible to get optical-to-X-ray spectral energy distribution of sources with simultaneous observations, thus bypassing the problems arising due to variability. The OM fluxes of our targets are listed in Table 8 while the X-ray fluxes are given in Tables 5 and 6. The optical to X-ray spectral energy distribution is often parametrized by α_{ox} as defined above (§5); the α_{ox} values of our targets are listed in Table 9. It is useful to note here that the OM observations are taken with one or more of optical/UV filters with central wavelengths at 2070Å, 2298Å, 2905Å. Thus the actual observations are taken at wavelengths close to 2500Å, at which the monochromatic optical flux is calculated in the stan-

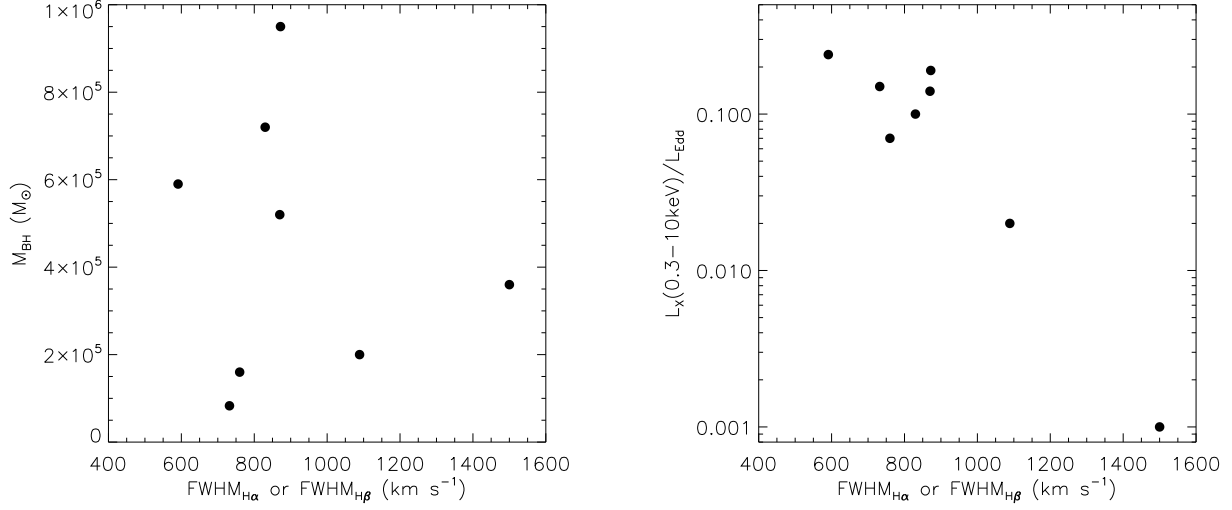


FIG. 11.— Black hole mass (*left panel*) and X-ray luminosity relative to the Eddington luminosity (*right panel*) as a function of FWHM of the Balmer H α or H β line.

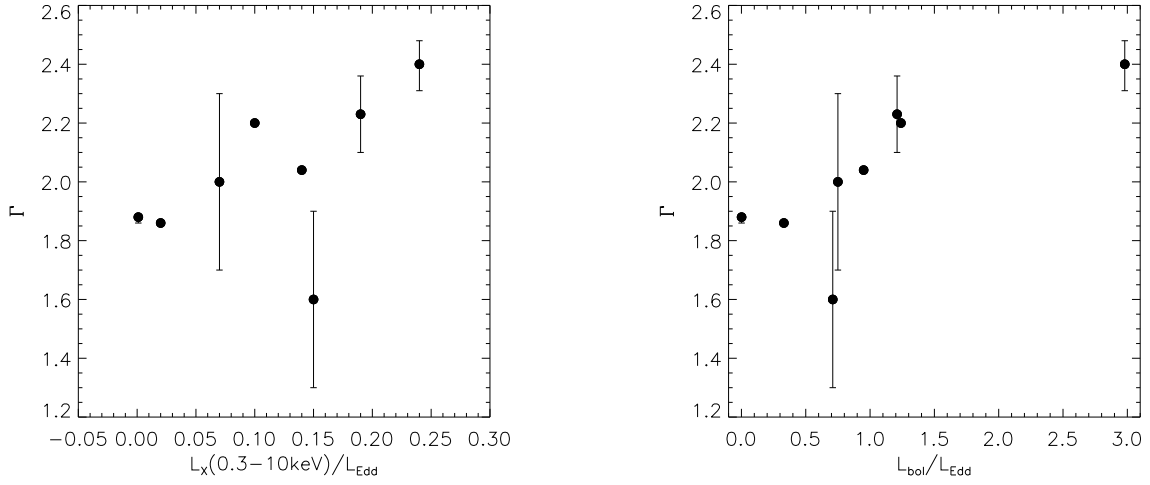


FIG. 12.— X-ray photon index Γ as a function of X-ray luminosity relative to the Eddington luminosity (*left panel*) and Eddington ratio (*right panel*).

standard α_{ox} definition. For this reason our measurements of $f_\nu(2500\text{\AA})$ are far more accurate than those calculated from extrapolations of longer wavelengths (e.g., Strateva et al. 2005). It is well known that AGNs are increasingly X-ray faint relative to UV, for higher luminosities. In Figure 13 we have plotted the α_{ox} vs. $L_\nu(2500\text{\AA})$ ($\text{erg s}^{-1} \text{Hz}^{-1}$). The Strateva et al. (2005) relation for the optically selected AGNs is shown by the solid line and our targets with IMBHs are shown as solid circles. Ours are all low luminosity sources; all AGNs in the Strateva et al. sample lie to the right of the vertical dotted line.

Our sample of IMBH AGNs extends the relation to lower luminosities. The horizontal line marks the lowest α_{ox} for $\log L_\nu < 28$ in the Strateva et al. data. While six of our sources appear to be consistent with the Strateva et al. relation, SDSS J1434+0338 and POX 52 are clearly X-ray weak. While broad absorption line quasars are often undetected in X-rays, and thus observed as X-ray faint, their intrinsic X-ray fluxes, corrected for absorption are usually similar to non-BALQSOs; Green & Mathur 1996), X-ray weakness of the two AGNs with IMBHs is not due to intrinsic absorption as the α_{ox} values were derived after correcting for the Galactic as well

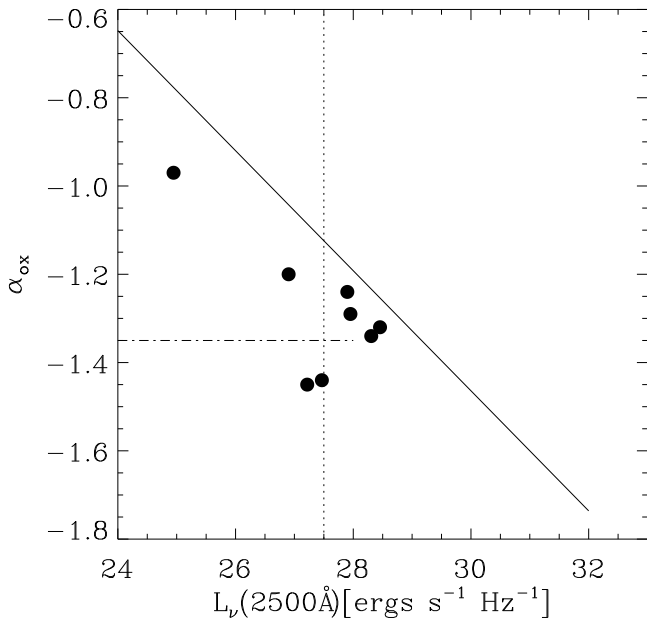


FIG. 13.— α_{ox} as a function of monochromatic luminosity at 2500Å for AGNs with IMBHs. The solid line represents the primary dependence of α_{ox} on $\log(L_{2500\text{Å}})$ ($\alpha_{ox} = -0.136\log L_{UV} + 2.616$) for a large sample of 195 AGNs (Strateva et al. 2005). The horizontal dash-dotted line represents the lower bounds to scatter in the $\alpha_{ox} - L_{\nu}$ relation for the 195 AGNs. The vertical dotted line marks the lower end of the $L_{\nu}(2500\text{Å})$ range in the large sample of Strateva et al. (2005)

any intrinsic neutral/warm absorption. It is worth noting that POX 52 and J1434+0338 are only mildly X-ray weak. NLS1 galaxies studied by Gallo et al. (2006) show a large range $-1.76 \leq \alpha_{ox} \leq -0.94$. Hence the optical-to-X-ray spectral energy distribution of all eight AGNs with IMBHs are entirely consistent with that of NLS1 galaxies.

NGC 4395 appears to be weak in the UV and bright in X-rays as it has largest α_{ox} among the IMBH AGNs. This is also evident from the L_X/L_{Edd} and L_{bol}/L_{Edd} values. While the contribution of 0.3 – 10 keV X-ray luminosity to the bolometric luminosity is only 6 – 21% for the six SDSS AGNs and POX 52, the contribution is $\sim 80\%$ in the case of NGC 4395. This may suggest different disk-corona geometries for NGC 4395 and other AGNs with IMBHs. If the accretion disk in NGC 4395 is truncated at large inner radii, then the disk is expected to be cooler and hence weaker optical/UV emission. Such truncated disks are thought to exist in the hard state of BHBs when the accretion rate is low (see e.g., Remillard & McClintock 2006). The lack of soft X-ray excess emission, low L/L_{Edd} , extremely rapid variability and the lack of UV emission are all consistent with a truncated disk and NGC 4395 is likely in a low state similar to the low/hard state of BHBs.

6.6. Nature of AGNs with IMBHs

The main objective of this study is to investigate the dependence of X-ray properties on BH mass and thereby

to identify any departure in the accretion process that may be related to the growing phase in the early evolution of BHs and galaxies. As shown above, though AGNs with IMBHs show strong X-ray variability, the excess variance – luminosity and the PDS break – BH mass relations are consistent with the variability properties of AGNs with SMBHs. The short break time scales are consistent with the low BH mass of AGNs with IMBHs. The primary X-ray continuum and the optical-to-X-ray spectral energy distributions are also similar to that observed from massive AGNs. The properties of neutral and warm absorbers in NGC 4395 and POX 52 are also not distinct when compared to that observed from Seyfert galaxies. Thus we conclude that the observed X-ray and UV properties of AGNs with IMBHs are consistent with the low BH mass extension of SMBHs in Seyfert galaxies and quasars. The accretion process in AGNs with IMBHs is similar to that in more massive AGNs. There is no clear indication of any departure in the observational characteristics that may be related to the early evolution of black holes and galaxies if the co-evolution of BHs and galaxies is not established in the early phases. This conclusion is consistent with the fact that two of AGNs NGC 4395 and POX 52 follow the same $M_{BH} - \sigma^*$ relation known for the massive AGNs and normal galaxies.

7. SUMMARY

We presented a systematic X-ray variability and spectral study of eight AGNs with IMBHs based on 12 *XMM-Newton* observations. The main results are as follows.

1. Strong X-ray variability is a general property of AGNs with IMBHs. The normalized excess variances of AGNs with IMBHs are the largest observed among radio-quiet AGNs. The excess variance – luminosity relation for AGNs with IMBHs is consistent with that of more massive AGNs.
2. The X-ray variability time scales of AGNs with IMBHs are the shortest observed from all radio-quiet AGNs, implying the most compact X-ray emitting regions in AGNs with IMBHs. The observed PDS breaks in AGNs with IMBHs are consistent with the well known $M_{BH} - T_{br}$ relation for AGNs and BHBs.
3. The shape of the 0.3–10 keV power-law continuum of AGNs with IMBHs is found to be in the range $\Gamma \sim 1.7 - 2.6$, entirely consistent with the range of photon indices observed from radio-quiet AGNs.
4. Only four of eight AGNs show clear evidence for soft X-ray excess emission similar to that observed from NLS1 galaxies. X-ray spectra of three other AGNs are consistent with the presence of the soft excess emission. NGC 4395 with the lowest $L/L_{Edd} \sim 0.001$ is the only AGN with IMBHs that clearly lacks strong soft excess emission. These observations imply that the black hole mass is not the primary driver for the origin of strong soft X-ray excess emission. High L/L_{Edd} is likely responsible for the strong soft X-ray excess emission from some AGNs.

5. The optical-to-X-ray spectral energy distributions of AGNs with IMBHs are generally consistent with that observed from narrow-line Seyfert 1 galaxies.
6. Two AGNs NGC 4395 and POX 52 show evidence for multiple absorbers – both neutral and warm. These absorbers are similar to that observed from Seyfert 1 galaxies.
7. NGC 4395 showed a remarkable X-ray spectral variability that is well explained by the variability in the partial covering neutral absorbers and the warm absorbers.
8. Irrespective of the X-ray photon index, the width of the optical Balmer lines $H\alpha$ or $H\beta$ of AGNs with IMBHs are narrow and these AGNs do not follow the correlation between the Γ of X-ray spectrum and the FWHM of the $H\beta$ line observed for NLS1 and BLS1 galaxies. This can be understood

if the primary driver of the width of $H\beta$ line and the shape of the primary X-ray continuum is not the black hole mass alone but the accretion rate relative to the Eddington rate.

9. The observed X-ray and UV properties of AGNs with IMBHs are consistent with these AGNs being the low mass extension of the more massive radio-quiet AGNs.

GCD gratefully acknowledges the support of NASA grant NNX06AE38G. This work is based on observations obtained with *XMM-Newton*, an ESA science mission with instruments and contributions directly funded by ESA Member States and the USA (NASA). This research has made use of data obtained through the High Energy Astrophysics Science Archive Research Center Online Service, provided by the NASA/Goddard Space Flight Center.

REFERENCES

- Abbrassart, A., & Czerny, B. 2000, *A&A*, 356, 475
- Barth, A. J., Ho, L. C., Rutledge, R. E., & Sargent, W. L. W. 2004, *ApJ*, 607, 90
- Blustin, A. J., Page, M. J., Fuerst, S. V., Branduardi-Raymont, G., & Ashton, C. E. 2005, *A&A*, 431, 111
- Bohlin, R. C., Savage, B. D., & Drake, J. F. 1978, *ApJ*, 224, 132
- Boller, T. 2006, *Astronomische Nachrichten*, 327, 1071
- Boller, T., Brandt, W. N., & Fink, H. 1996, *A&A*, 305, 53
- Boller, T., Fabian, A. C., Sunyaev, R., Trümper, J., Vaughan, S., Ballantyne, D. R., Brandt, W. N., Keil, R., & Iwasawa, K. 2002, *MNRAS*, 329, L1
- Brandt, W. N., Mathur, S., & Elvis, M. 1997, *MNRAS*, 285, L25
- Cardelli, J. A., Clayton, G. C., & Mathis, J. S. 1989, *ApJ*, 345, 245
- Dewangan, G. C. 2002, *ApJ*, 581, L71
- Di Matteo, T., Croft, R. A. C., Springel, V., & Hernquist, L. 2003, *ApJ*, 593, 56
- Elvis, M. 2000, *ApJ*, 545, 63
- Ferland, G. J., Korista, K. T., Verner, D. A., Ferguson, J. W., Kingdon, J. B., & Verner, E. M. 1998, *PASP*, 110, 761
- Filippenko, A. V., & Ho, L. C. 2003, *ApJ*, 588, L13
- Gallo, L. C., Tanaka, Y., Boller, T., Fabian, A. C., Vaughan, S., & Brandt, W. N. 2004, *MNRAS*, 353, 1064
- Green, P. J., & Mathur, S. 1996, *ApJ*, 462, 637
- Greene, J. E., & Ho, L. C. 2004, *ApJ*, 610, 722
- . 2007a, *ArXiv e-prints*, 707
- . 2007b, *ApJ*, 656, 84
- Grupe, D., Komossa, S., & Gallo, L. C. 2007, *ApJ*, 668, L111
- Grupe, D., Mathur, S., & Komossa, S. 2004a, *AJ*, 127, 3161
- Grupe, D., Wills, B. J., Leighly, K. M., & Meusinger, H. 2004b, *AJ*, 127, 156
- Gu, M. F., Holzer, T., Behar, E., & Kahn, S. M. 2006, *ApJ*, 641, 1227
- Holt, S. S., Mushotzky, R. F., Boldt, E. A., Serlemitsos, P. J., Becker, R. H., Szymkowiak, A. E., & White, N. E. 1980, *ApJ*, 241, L13
- Hughes, S. A. 2002, *MNRAS*, 331, 805
- Iwasawa, K., Fabian, A. C., Almaini, O., Lira, P., Lawrence, A., Hayashida, K., & Inoue, H. 2000, *MNRAS*, 318, 879
- Kaspi, S., Smith, P. S., Netzer, H., Maoz, D., Jannuzi, B. T., & Giveon, U. 2000, *ApJ*, 533, 631
- Kunth, D., Sargent, W. L. W., & Bothun, G. D. 1987, *AJ*, 93, 29
- Kunth, D., Sargent, W. L. W., & Kowal, C. 1981, *A&AS*, 44, 229
- Leighly, K. M. 1999a, *ApJS*, 125, 297
- . 1999b, *ApJS*, 125, 317
- McHardy, I. M., Gunn, K. F., Uttley, P., & Goad, M. R. 2005, *MNRAS*, 359, 1469
- McHardy, I. M., Koerding, E., Knigge, C., Uttley, P., & Fender, R. P. 2006, *Nature*, 444, 730
- Nandra, K., George, I. M., Mushotzky, R. F., Turner, T. J., & Yaqoob, T. 1997, *ApJ*, 476, 70
- Osterbrock, D. E., & Pogge, R. W. 1985, *ApJ*, 297, 166
- Papadakis, I. E., & Lawrence, A. 1993, *MNRAS*, 261, 612
- Peterson, B. M., Bentz, M. C., Desroches, L.-B., Filippenko, A. V., Ho, L. C., Kaspi, S., Laor, A., Maoz, D., Moran, E. C., Pogge, R. W., & Quillen, A. C. 2005, *ApJ*, 632, 799
- Porter, R. L., Ferland, G. J., Kraemer, S. B., Armentrout, B. K., Arnaud, K. A., & Turner, T. J. 2006, *PASP*, 118, 920
- Proga, D. 2007, *ApJ*, 661, 693
- Remillard, R. A., & McClintock, J. E. 2006, *ARA&A*, 44, 49
- Strateva, I. V., Brandt, W. N., Schneider, D. P., Vanden Berk, D. G., & Vignali, C. 2005, *AJ*, 130, 387
- Strüder, L., Briel, U., Dennerl, K., Hartmann, R., Kendziorra, E., Meidinger, N., Pfeffermann, E., Reppin, C., Aschenbach, B., Bornemann, W., Bräuninger, H., Burkert, W., Elender, M., Freyberg, M., Haberl, F., Hartner, G., Heuschmann, F., Hippmann, H., Kastelic, E., Kemmer, S., Kettenring, G., Kink, W., Krause, N., Müller, S., Oppitz, A., Pietsch, W., Popp, M., Predehl, P., Read, A., Stephan, K. H., Stötter, D., Trümper, J., Holl, P., Kemmer, J., Soltau, H., Stötter, R., Weber, U., Weichert, U., von Zanthier, C., Carathanassis, D., Lutz, G., Richter, R. H., Solc, P., Böttcher, H., Kuster, M., Staubert, R., Abbey, A., Holland, A., Turner, M., Balasini, M., Bignami, G. F., La Palombara, N., Villa, G., Buttler, W., Gianini, F., Lainé, R., Lumb, D., & Dhez, P. 2001, *A&A*, 365, L18
- Turner, M. J. L., Abbey, A., Arnaud, M., Balasini, M., Barbera, M., Belsole, E., Bennie, P. J., Bernard, J. P., Bignami, G. F., Boer, M., Briel, U., Butler, I., Cara, C., Chabaud, C., Cole, R., Collura, A., Conte, M., Cros, A., Denby, M., Dhez, P., Di Coco, G., Dowson, J., Ferrando, P., Ghizzardi, S., Gianotti, F., Goodall, C. V., Gretton, L., Griffiths, R. G., Hainaut, O., Hochedez, J. F., Holland, A. D., Jourdain, E., Kendziorra, E., Lagostina, A., Laine, R., La Palombara, N., Lortholary, M., Lumb, D., Marty, P., Molendi, S., Pigot, C., Poindron, E., Pounds, K. A., Reeves, J. N., Reppin, C., Rothenflug, R., Salvétat, P., Sauvageot, J. L., Schmitt, D., Sembay, S., Short, A. D. T., Spragg, J., Stephen, J., Strüder, L., Tiengo, A., Trifoglio, M., Trümper, J., Vercellone, S., Vigroux, L., Villa, G., Ward, M. J., Whitehead, S., & Zonca, E. 2001, *A&A*, 365, L27
- Uttley, P., & McHardy, I. M. 2005, *MNRAS*, 363, 586
- Vaughan, S., Iwasawa, K., Fabian, A. C., & Hayashida, K. 2005, *MNRAS*, 356, 524
- Vaughan, S., Reeves, J., Warwick, R., & Edelson, R. 1999, *MNRAS*, 309, 113
- Williams, R. J., Mathur, S., & Pogge, R. W. 2004, *ApJ*, 610, 737